AN EXPERIMENTAL STUDY OF THE REACTION

$$\pi^0 + p \rightarrow \rho^0 + p \text{ AT } 15.0 \text{ GeV/c}^*$$

WILLIAM TYLER KAUNE

STANFORD LINEAR ACCELERATOR CENTER

STANFORD UNIVERSITY

Stanford, California 94305

---

*Ph.D. dissertation.

ABSTRACT

The <u>only</u> one-particle t-channel exchange mechanism which is thought to con-
tribute to the reaction $\pi^0 + p \to \rho^0 + p$ involves the exchange of a ω meson. We
use our measurements of the differential cross sections and density matrices
of the reactions $\pi^{\pm} + p \to \rho^{\pm} + p$ and $\pi^- + p \to \rho^0 + n$ to calculate the differential
cross section and density matrix for $\pi^0 + p \to \rho^0 + p$ at 15.0 GeV/c.

To make the required measurements a new technique was developed using
optical spark chambers to view the decay products of the ρ mesons. The re-
coil proton was viewed for events where the square momentum transfer to the
proton exceeded about .04 $(GeV/c)^2$. In the experiment, conducted at the
Stanford Linear Accelerator Center, we obtained at 15.0 GeV/c 811 events
from the channel $\pi^+ + p \to \rho^+ + p$, 772 from $\pi^- + p \to \rho^- + p$, and 817 from
$\pi^- + p \to \rho^0 + n$.

We present the differential cross sections and density matrix elements for
these three channels. The energy dependence of these quantities is determined
by including data from other experiments.

The differential cross section and density matrix elements for the reaction
$\pi^0 + p \to \rho^0 + p$ at 15.0 GeV/c are calculated. This data has the general fea-
tures expected in a reaction dominated by ω-exchange but fails to agree in the
region $|t| \lesssim 0.3$ $(GeV/c)^2$ with a detailed calculation based on the dual-absorption
model.

A test of the vector dominance model is performed by comparing the two
reactions $\gamma + p \to \rho^0 + p$ and $\pi^0 + p \to \rho^0 + p$. We find agreement in shape but
an overall normalization difference consistent only with a significantly lower
value of $\gamma_\rho^2/4\pi$.

ACKNOWLEDGEMENTS

TABLE OF CONTENTS

LIST OF TABLES

LIST OF FIGURES

CHAPTER I

INTRODUCTION AND GENERAL CONSIDERATIONS

A. <u>Physics of $\pi^0 + p \rightarrow \rho^0 + p$</u>

Our theoretical analysis will be based on the t-channel exchange model for two-body reactions—a model which is illustrated in Fig. 1. The effect on this model of absorption corrections is discussed briefly in Chapter V.

Only* $I^G = 0^-$ and $I^G = 1^-$ non strange bosons can contribute, in this approximation, to the general class of ρ production reactions $\pi + p \rightarrow \rho + N$. This is also illustrated in Fig. 1.
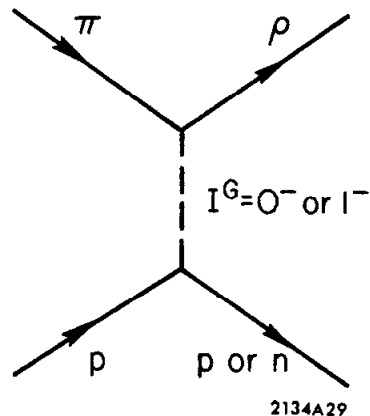
FIG. 1—Feynman diagram showing possible t-channel
exchanges in the reactions $\pi N \rightarrow \rho N$.

Considerable experimental effort[1,2] has been devoted to the particular channel $\pi^- + p \rightarrow \rho^0 + n$ which can only have terms involving π, A_1 and A_2 exchange, the known $I^G = 1^-$ non strange bosons. The π has, by far, the lightest mass and has been expected to be the dominant exchange at small momentum transfer in this particular channel, but recently very high statistics experiments[2] have found behavior that can be explained by A_2 exchange for $|t|$ as low as $0.1(GeV/c)^2$.

*I stands for isospin.

It has only recently been realized[3] that the isolation of the $I^G = 0^-$ exchange mechanisms is also possible, through the indirect study of the reaction $\pi^o + p \rightarrow \rho^o + p$. It is very easy to show that the amplitudes for $\pi^o + p \rightarrow \rho^o + p$ involving $I^G = 1^-$ exchanges are zero, for the boson vertex in Fig. 1 would involve the coupling of two $I = 1$ particles, both with $I_3 = 0$, to form a $I = 1$, $I_3 = 0$ state (the ρ^o) and the Clebsch-Gordan coefficient for this combination is zero.

The only known mesons that can contribute to $\pi^o + p \rightarrow \rho^o + p$ are the ω and ϕ. Further it is known that the coupling of the ϕ to the NN system is small[4] and in this case is negligible[5]. Thus, the reaction $\pi^o + p \rightarrow \rho^o + p$, in this approximation, is an example of the exchange of a single particle, the spin-1 ω meson.

In Chapter V our measurements of $\pi^o + p \rightarrow \rho^o + p$ will be examined in this context. In particular, the effects of absorption mechanisms will be discussed; and a test for ω-exchange, valid even when absorption is present, will be applied to the data. Also, by using the lower energy measurements, the energy dependence of the reaction $\pi^o + p \rightarrow \rho^o + p$ and, thus, of the ω-trajectory will be determined.

Quite apart from the previous considerations, the reaction $\pi^o + p \rightarrow \rho^o + p$ is interesting because of its connection, through the Vector Dominance Model, to the reaction $\gamma + p \rightarrow \pi^o + p$. In Chapter V, we shall examine this connection.

B. Method to Measure $\pi^o + p \rightarrow \rho^o + p$

Since a direct measurement is not, at this time, possible, we have used an indirect method based on isospin conservation. Let $A_{\mu \lambda_N} (\pi p \rightarrow \rho N)$ be

the amplitude to produce a ρ with helicity μ where the nucleon helicities are collectively denoted λ_N. The following equations result from an isospin analysis in the s-channel.

$$A_{\mu\lambda_N}(\pi^+ p \to \rho^+ p) = A_{\mu\lambda_N}^{3/2}$$

$$A_{\mu\lambda_N}(\pi^- p \to \rho^- p) = \frac{1}{3} A_{\mu\lambda_N}^{3/2} + \frac{2}{3} A_{\mu\lambda_N}^{1/2}$$

$$A_{\mu\lambda_N}(\pi^- p \to \rho^0 n) = \frac{\sqrt{2}}{3} A_{\mu\lambda_N}^{3/2} - \frac{\sqrt{2}}{3} A_{\mu\lambda_N}^{1/2}$$

$$A_{\mu\lambda_N}(\pi^0 p \to \rho^0 p) = \frac{2}{3} A_{\mu\lambda_N}^{3/2} + \frac{1}{3} A_{\mu\lambda_N}^{1/3}$$

$A_{\mu\lambda_N}^{3/2}$ and $A_{\mu\lambda_N}^{1/2}$ are the isospin $\frac{3}{2}$ and $\frac{1}{2}$ amplitudes which, assuming isospin conservation, depend only on the total isospin. Then

$$A_{\mu\lambda_N} A^*_{\nu\lambda_N} (\pi^0 p \to \rho^0 p) = \frac{1}{2} \left[A_{\mu\lambda_N} A^*_{\nu\lambda_N} (\pi^+ p \to \rho^+ p) \right.$$

$$\left. + A_{\mu\lambda_N} A^*_{\nu\lambda_N} (\pi^- p \to \rho^- p) - A_{\mu\lambda_N} A^*_{\nu\lambda_N} (\pi^- p \to \rho^0 n) \right].$$

$$\tag{1.1}$$

It is conventional to introduce the density matrix defined by

$$\rho_{\mu\nu}^H \frac{d\sigma}{dt} = \sum_{\lambda_N} A_{\mu\lambda_N} A^*_{\nu\lambda_N} . \tag{1.2}$$

The element $\rho_{\mu\mu}^H$ is the probability of finding the ρ, once it is produced, with helicity μ. The normalization condition is

$$\sum_{\mu} \rho_{\mu\mu}^{H} = 1 \, .$$

In terms of the density matrix Eq. (1.1) becomes

$$\rho_{\mu\nu}^{H} \frac{d\sigma}{dt} (\pi^{0}p \to \rho^{0}p) = \frac{1}{2} \left[\rho_{\mu\nu}^{H} \frac{d\sigma}{dt} (\pi^{+}p \to \rho^{+}p) \right.$$

$$\left. + \rho_{\mu\nu}^{H} \frac{d\sigma}{dt} (\pi^{-}p \to \rho^{-}p) - \rho_{\mu\nu}^{H} \frac{d\sigma}{dt} (\pi^{-}p \to \rho^{0}n) \right]$$

(1.3)

Setting $\mu = \nu$ and summing gives

$$\frac{d\sigma}{dt} (\pi^{0}p \to \rho^{0}p) = \frac{1}{2} \left[\frac{d\sigma}{dt} (\pi^{+}p \to \rho^{+}p) + \frac{d\sigma}{dt} (\pi^{-}p \to \rho^{-}p) - \frac{d\sigma}{dt} (\pi^{-}p \to \rho^{0}n) \right]$$

(1.4)

Equations (1.3) and (1.4) represent a complete prescription for extracting the cross section and density matrix elements for the reaction $\pi^{0} + p \to \rho^{0} + p$ from measurements of the reactions

$$\pi^{\pm} + p \to \rho^{\pm} + p$$
$$\pi^{-} + p \to \rho^{0} + n \, .$$

(1.5)

Experimentally, the ρ is observed indirectly through the decay $\rho \to \pi + \pi$. Using the experimental measurement of the $\pi\pi$ four-momentum the four variables of interest can be calculated. These are: t, the square of the four-momentum transfer to the ρ; $M_{\pi\pi}$, the invariant mass of the $\pi\pi$ system and of the ρ; and $\cos \Theta_{\rho}^{*}$ and Φ_{ρ}^{*}, the spherical angles of the $\pi\pi$ pair in the $\pi\pi$ rest frame. We shall hereafter refer to this set of four variables as the "physics variables."

C. Present Experimental Status

To this date, three experiments have been reported which study the .

- 4 -

reaction $\pi^0 + p \rightarrow \rho^0 + p$. All have used bubble chambers as their means

of particle detection. Michael and Gidal[6] have studied the reaction

$\pi^+ + p \rightarrow \rho^+ + p$ at 2.67 GeV/c. By combining this measurement with sim-

ilar measurements[7] using a π^- beam the cross sections and density matrix

elements for $\pi^0 + p \rightarrow \rho^0 + p$ were obtained. Michael and Gidal have sep-

arated the $\pi^0 + p \rightarrow \rho^0 + p$ cross section into natural and unnatural parity

exchange components and, at small-t, find significant unnatural parity

contributions, rather surprising as the ω is a natural parity particle.

However, this experiment does use data from two distinct measurements

to isolate the reaction $\pi^0 + p \rightarrow \rho^0 + p$ with Eq. (1.3) and Eq. (1.4) and

is highly sensitive to any relative normalization errors.

A 6.0 GeV/c experiment[8] at Brookhaven has used the same apparatus

to measure all three of the reactions (1.5). The authors conclude that

their results are consistent with pure ω-exchange in the reaction $\pi^0 + p \rightarrow$

$\rho^0 + p$, in definite contrast to the 2.67 GeV/c data. The authors fit

$\frac{d\sigma}{dt}(\pi^0 p \rightarrow \rho^0 p)$ with the form

$$\frac{d\sigma}{dt}(\pi^0 p \rightarrow \rho^0 p) = A\, e^{2bt} J_1^2\, (r\sqrt{-t})\, (1 + \tan^2 \frac{\pi}{2}\, \alpha) \qquad (1.6)$$

which is suggested by the dual-absorption model of Harari[9]; r is related to

the scattering radius of the proton and is ≈ 1 fm by their fit.

Finally, a recent experiment at CERN[10] has appeared. These authors

have studied all three reactions (1.5) at 16.0 GeV/c and obtained the cross

section and density matrix for $\pi^0 + p \rightarrow \rho^0 + p$. This experiment, in con-

trast to the 6.0 (GeV/c) results, but in agreement with the 2.67 (GeV/c) data,

finds a non-zero contribution from the exchange of an unnatural parity particle.

They also fit their data with the dual-absorption model form of Eq. (1.6).

At this point there is no consistent interpretation of these results. All three experiments show results qualitatively in agreement with the form of Eq. (1.6), but differing amounts of unnatural parity contribution. More experimental information is needed. Further, there are compelling reasons to attempt the experiment using different experimental techniques.

D. Choice of Apparatus; General Considerations

In studying the reactions $\pi^{\pm} + p \to \rho^{\pm} + p$ bubble chambers have an intrinsic difficulty for small values of t. The π^{o} from the ρ decay is not detected so the recoil proton must be detected, which at low values of t is difficult because of the short proton range. This bias becomes serious for $|t| \leq 0.1$ (GeV/c)^2 [8,11]. All the bubble chamber experiments discussed in Section C have observed pronounced dips in $\frac{d\sigma}{dt}$ $(\pi^{o}p \to \rho^{o}p)$. These dips are suggested by the dual-absorption model[9] but may, in fact, be attributable to scanning biases in the $\pi^{\pm} + p \to \rho^{\pm} + p$ data.

To overcome this difficulty we developed a new method of investigating the reactions $\pi^{\pm} + p \to \rho^{\pm} + p$. An optical spark chamber system was designed to detect both the $\pi^{\pm}$ and π^{o}, through the decay of $\pi^{o} \to \gamma + \gamma$; no longer is it necessary to detect the recoil proton. However, a different type of problem, again associated with small-t values, may occur.

In this method the four-momentum of the $\pi^{\pm}$ and the angles of the two photons are measured. To reconstruct the recoil four-momentum and the two photon energies at all one must assume that the recoil system is, in fact, a proton and that the two photons do, in fact, come from the decay $\pi^{o} \to \gamma + \gamma$, and even then two solutions for the unmeasured variables result because of the identical nature of the two photons; this is the so-called π^{o} ambiguity.

In order for us to observe a $\pi^{\pm}$ and two photons and yet mistakenly label the recoil particle as a proton or mistakenly assume the photons come from one π^{o} decay, additional particles must have been produced; for example the recoil system might have been a Δ^{+} (1238). Our solution is to detect these additional particles with high efficiency either in the spark chambers or in an extensive veto counter system, both sensitive to charged particles and photons. We then veto these events either optically from extra spark chamber tracks or electronically. In addition, we provided spark chambers to detect the recoil proton when it was able to penetrate the hydrogen target and support structure. For $|t| > .08 \ (GeV/c)^2$ the proton was always observed.

This proton measurement also allowed us to resolve the π^{o} ambiguity. When the proton was not observed other information was required. In about half the cases the mere knowledge that the proton was not seen, hence that $|t| \lesssim .08 \ (GeV/c)^2$ was sufficient. Otherwise we determined the relative energies of the two photons from the spark chamber data.

CHAPTER II

APPARATUS

A.   General Description

The two final states of interest in this experiment, corresponding to the $\rho^{\pm}$ and ρ^{0}, are $\pi^{\pm} \gamma\gamma p$ and $\pi^{+}\pi^{-} n$. To detect these we built the apparatus shown in Fig. 2, consisting of eight functionally distinct sections. The beam delivered positive or negative charged pions of known momentum to the liquid hydrogen target. Fast forward secondary charged particles were detected and momentum analyzed in the charged particle spectrometer consisting of optical spark chambers T_1, T_2, T_3, a large magnet, and scintillation counter hodoscopes CT and RG. Photons were detected by the π^0 detector consisting of T_2, T_3, T_4, and scintillation counters FG and RG. Protons escaping the target were detected by the proton spectrometer. The veto system consisting of scintillation counters TV, DV, and A_3 detected most charged particles and photons which were missed by the above systems. The optics system enabled us to accurately record the data. The electronics system generated a trigger if the scintillation counter information met predefined criteria, operated the spark chambers and camera, and recorded the scintillation counter information for later use.

These systems are discussed in detail in the following sections of this chapter; in the last section the performance of the apparatus is discussed.

B.   Beam

Pions, along with electrons, kaons, and muons, were produced by passing the SLAC 18.0 GeV/c electron beam through a 1 radiation length
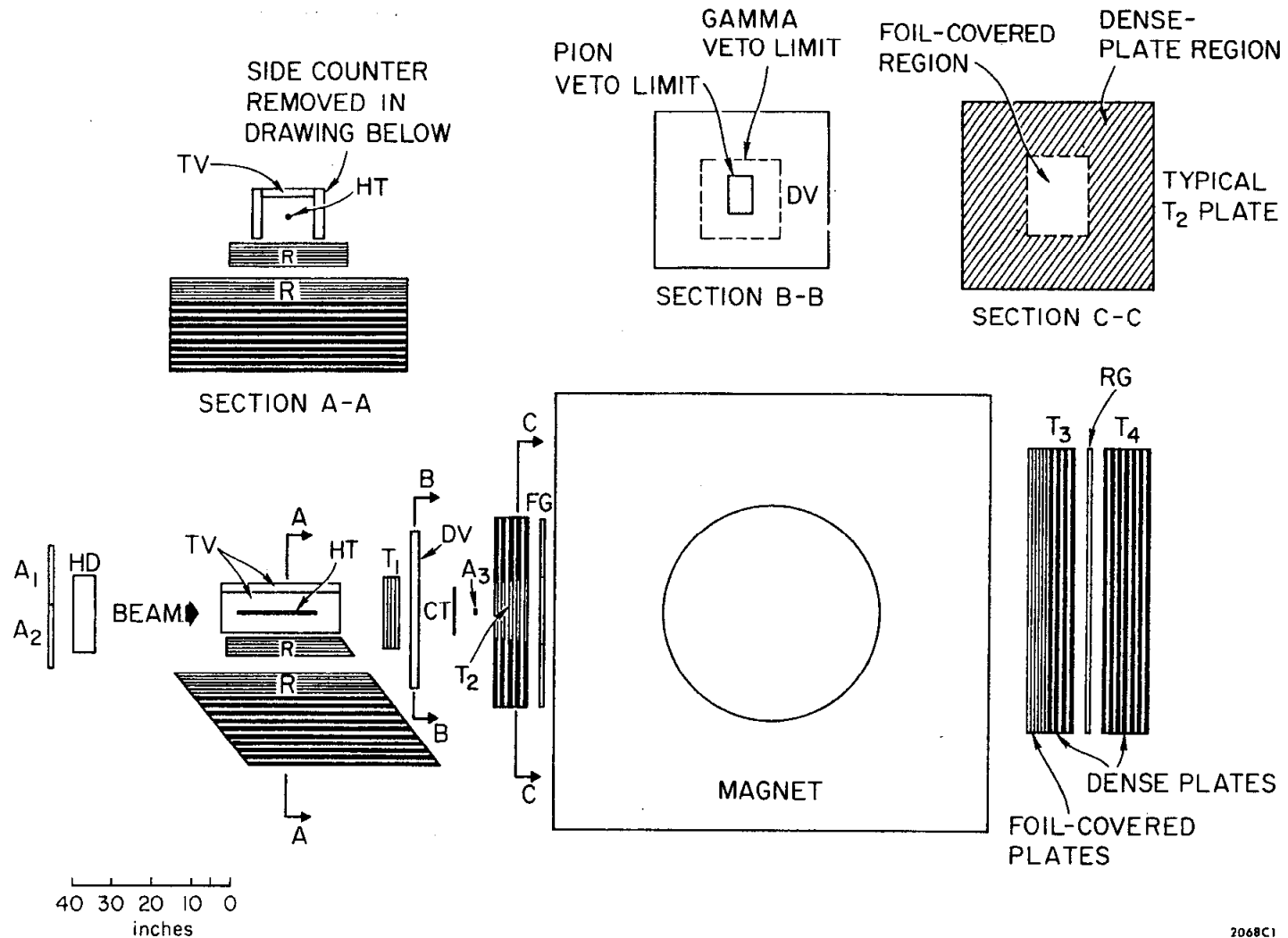
FIG. 2--Elevation view of the apparatus.

beryllium rod. We accepted particles at an average angle of 1^O to the primary electron beam. The first two stages selected a momentum bite of $\pm 0.5\%$. The beam was brought to an achromatic focus at the end of the second stage. Here a small trigger counter (B_1) was placed along with a lead brick collimator to suppress halo particles. The third stage of the beam carried the beam forward to a focus at the hydrogen target. A large counter (HD) was positioned 1.5 m upstream of the hydrogen target. Finally, 1.2 m upstream of the target, we placed a very large veto counter, A_1A_2, with a small hole through which the beam passed. This counter vetoed all particles which would have missed the 2 cm diameter hydrogen target. A good beam particle was signalled by the combination $B_1 \cdot HD \cdot \overline{A_1A_2}$.

The phase space of the beam was measured with small optical spark chambers. The beam measures (FWHM) .45 cm wide by .55 cm high with an angular phase space of 2.0 mrad by 2.25 mrad.

The electron contamination in the beam was initially large ($e^-/\pi^- \approx 50$) but was reduced to $< 0.1\%$ by the insertion of 2.0 radiation lengths of lead at the momentum focus. The $\mu^\pm$ contamination in the beam was determined with a μ telescope containing 1.95 m of iron to filter out all hadrons. The contamination for both the π^+ and π^- beam was found to be $3.5 \pm 0.5\%$. The contamination of $K^\pm$ was easily found as our apparatus detected the decay $K^\pm \rightarrow \pi^\pm + \pi^O$ in the vicinity of the hydrogen target. The K^+ contamination in the π^+ beam was $.84 \pm .10\%$ and the K^- contamination in the π^- beam $.25 \pm .05\%$.

The contamination of p and $\bar{p}$ was not measured. However, the results obtained for the SLAC 82" bubble chamber π beam can be applied to our beam.

Thus, the p contamination to the π^+ beam[12] was approximately $0.6 \pm 0.2\%$; the $\bar{p}$ contamination to the π^- beam [13] was negligible.

C.   Liquid Hydrogen Target

Fig. 3 shows the target structure from the side and in cross section. The hydrogen cell was made from clear 0.006" thick mylar in the form of a circular cylinder 50 cm long and 2.0 cm in diameter. The cell was enclosed in an aluminum-mylar vacumn jacket. The downstream end of this structure was a .040" aluminum dome. The top and sides of the target enclosure were made from .040" aluminum. To escape the target and its structure in these directions a proton required at least 35 MeV kinetic energy $\left(|t| > .07 \; (GeV/c)^2 \right)$. The bottom of the target structure was made from .010" mylar; the minimum kinetic energy required to escape was 20 MeV for a proton, corresponding to an event with $|t| \sim .035 \; (GeV/c)^2$.

D.   Charged Particle Spectrometer

The momentum and scattering angle of fast forward charged particles were determined with a large magnet and spark chambers T_1, T_2, and T_3 (see Fig. 2). The SLAC 54" pole diameter magnet was used with the gap width set to 36" and the vertically bending field set to yield $\int Bdl = 27$ kg-m.

Two spark chambers, T_1 and T_2, detected charged particles before entry into the magnet. T_1 contained seven plates 12" by 12". Each plate was made of two layers of .001" aluminum foil; we call these thin plates. The gaps between plates in all chambers were 3/8" wide. T_2 consisted of 13 plates, 4' x 4'. The upstream three were thin plates. Each of the downstream 10 plates was made from three 1/8" x 4' x 4' stainless steel plates glued together. A rectangular region through the center of each plate was

HYDROGEN TARGET

FLASK SUPPORT
DETAIL TOP VIEW

SECTION A-A

CARBON RESISTOR
(TOP AND BOTTOM)

WALL (0.040" ALUMINUM)

SUPERINSULATION

HEAT SHIELD (ALUMINUM)

SUPERINSULATION

FLASK (0.003" MYLAR)

BEAM OPENING

HYDROGEN
FLASK

MOUNTING
PLATE

FILL / RETURN LINES
(ALUMINUM TUBING)

WINDOW (0.010" MYLAR)

BEAM WINDOW
(0.010" MYLAR)

DEWAR CONNECTION

HYDROGEN FLASK

A

VIEWING PORT
(TYP.)

BEAM →

SUPPORT STRUCTURE

A

2156CI

FIG. 3--The LH$_2$ target and supporting structure.

cut out, then both sides covered with .001" aluminum foil. Thus, the central region of these plates formed a thin plate chamber while the outer region formed a thick plate chamber. These rectangular holes varied smoothly in size from 9.5" wide by 17.4" high for the upstream plate to 10.9" by 19.9" for the downstream plate. Mylar patches were used to deaden T_1 and T_2 to beam particles. This technique was moderately successful.

Charged particles exiting the magnet were detected in the first seven plates of T_3 which were 4' x 6' thin plates. Mylar patches deadened these plates to the beam.

The number of charged particles upstream of the magnet was counted by a 16 element scintillation counter hodoscope CT shown in Fig. 4. Charged particles downstream of the magnet were detected by a second hodoscope RG, placed between T_3 and T_4. About 20% of these charged hadrons interacted in the downstream 10 thick plates of T_3 and fired additional RG counters. The RG hodoscope is also shown in Fig. 4.

E. π^o Detector

π^o mesons were detected by converting the two photons from their decay in thick plate spark chambers. In about 70% of our events both photons passed through the inner thin plate sections of T_2, through the magnet, through the first seven (thin) plates of T_3, and into the thick plate sections of T_3 and T_4. T_3 contained 10 thick plates made by laminating a .10" sheet of lead between two .13" thick aluminum sheets; these units were 4' wide by 6' high, and each plate totaled .52 radiation lengths of matter. T_4 consisted of 17 thick plates identical in construction to the thick plates of T_3. Between T_3 and T_4 we placed a 1" thick stainless steel plate and the scintillation counter hodoscope RG. The total amount of matter in this system was 15.4

- 13 -

(a) CT HODOSCOPE

1"

8"

TO 56AVP PHOTOTUBES

BEAM HOLE

1/8" NE102 SCINITJLLATOR

(b) RGT HODOSCOPE

TO 56AVP PHOTOTUBES

42"

3/8" NE110 SCINTIL-LATOR

6"

BEAM HOLE

TO 56AVP PHOTOTUBES

(c) FGT HODOSCOPE

TO 56AVP PHOTOTUBES

3/8" NE110 SCINTIL-LATOR

CHARGED PARTICLE APERTURE

BEAM

TO 56AVP PHOTO-TUBES

40"
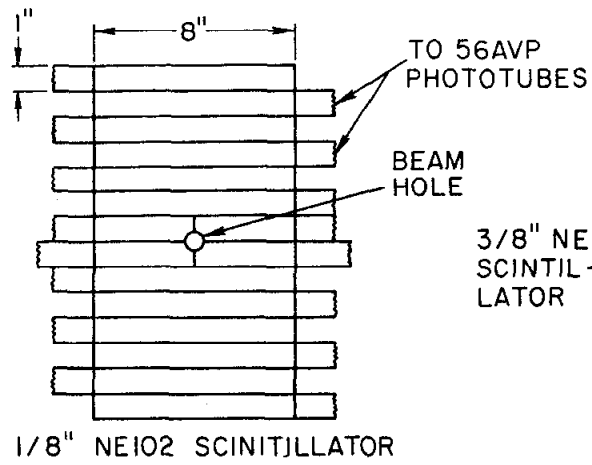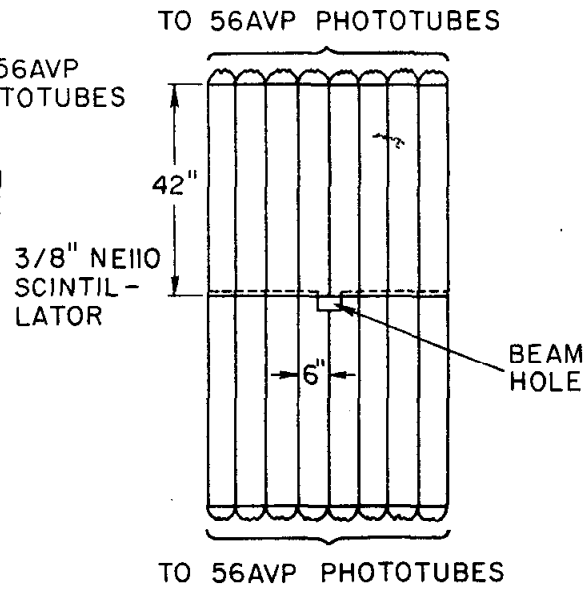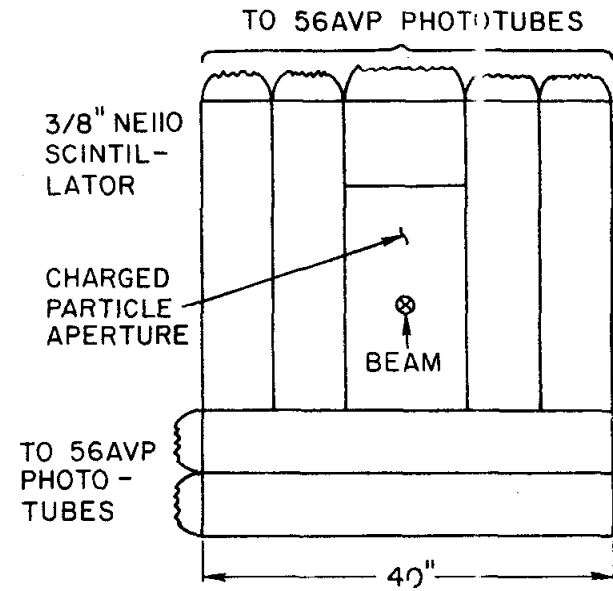
2134C5

FIG. 4--Trigger counter hodoscopes.

radiation lengths. The RG counters detected charged particles and photons, via their showers.

Since the typical $\rho^{\pm}$ event had one charged particle and two electromagnetic showers in T_3/T_4, we made extensive efforts to insure high multi-track chamber efficiency. The lamination process, described in the previous paragraph, was developed to produce flat, smooth plates; this was desirable, we thought, to prevent spurious sparks from robbing good sparks. We produced smooth plates, but with occasional bows of as much as .050". This did not noticeably degrade the performance of the chamber. To insure that there was ample electrical energy available we used very large electrical capacitors and very high voltages. Each chamber divided into pairs of electrically independent gaps. Each pair of gaps was equipped with 20,000 pfd of capacity and operated at about 15,000 volts. The total electrical energy stored for each chamber was 18 joules.

Photons at larger angles to the beam were detected in the steel sections of T_2. As discussed in Section D of this chapter, the downstream 10 plates of T_2 were 3/8" stainless steel (5.3 radiation length total) with rectangular holes through the middle. Behind the steel section of T_2 we positioned a scintillation counter hodoscope FG, shown in detail in Fig. 4.

F.   Proton Spectrometer

This system consisted of two spark chambers placed beneath the target; as mentioned in Section C, protons from events with $|t| \gtrsim .04 \ (GeV/c)^2$ and heading downwards were able to escape the target and its associated struc-ture. The seven thin plates of R_1 (Fig. 2) and the upper seven thin plates of R_2 measured the proton recoil angle. The lower 24 plates of R_2 were made

of aluminum sheet enclosed on both sides with aluminum foil. This could, in principle, provide a measure of the proton's momentum through its range; in this experiment only the proton angle measurement was used.

G.   Veto Counters

As mentioned in Chapter I an extensive veto system was of crucial importance to suppress contaminations. Surrounding the hydrogen target on the three sides not covered by the proton spectrometer were placed four-layer lead-scintillator sandwich counters (TV in Fig. 2). These units are shown in detail in Fig. 5. Between the target and the inner TV counter we placed 0.050" of lead in addition to the .16" of aluminum in the TV and target structure to suppress accidental vetoes from knock-on electrons coming from the hydrogen target. Approximately 37 MeV of kinetic energy was required for a proton to reach and fire a TV. Thus, events with $|t| \gtrsim .07$ $(GeV/e)^2$ were either vetoed or seen in the proton spectrometer.

Downstream of the target we placed a second veto system named the DV. This consisted of two layers of scintillator separated by lead and aluminum, totalling 2.4 radiation lengths. This unit is shown in detail in Fig. 6. An inner rectangular hole about 7" by 10" allowed charged particles to pass through while a larger hole in the lead-aluminum layer and in the downstream counter plane allowed photons to proceed to the thick plate of T_3/T_4 and to the thick plate sections of T_2.

Finally, we placed a small counter (A_3 in Fig. 2) in the beam 1.0 meter downstream of the hydrogen target. A good $\rho^\pm$ or ρ^0 event had no count in A_3.

SIDE VIEW

8.5"

TARGET FLASK   BEAM

LIGHT PIPE TO 56AVP PHOTOMULTIPLIER,
ONE EACH SCINTILLATOR

30" × 12" × 1/4" "PILOT Y" SCINTILLATOR

CROSS SECTION

TARGET FLASK

12"

LEAD
0.23 RL
0.77 RL
1.20 RL
1.50 RL

2156C4
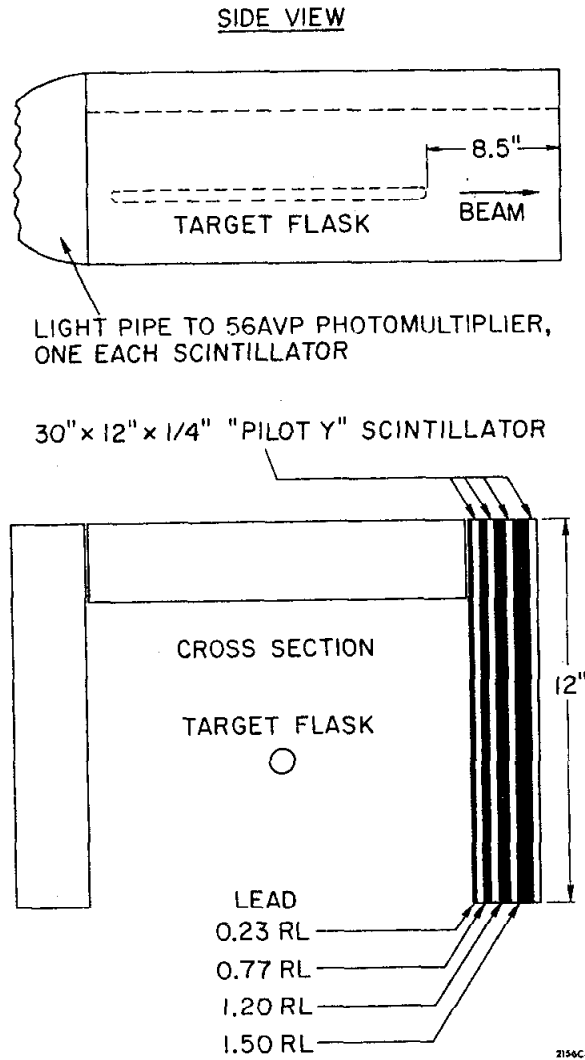
FIG. 5--Elevation and cross-sectional views of the target
veto lead-scintillator sandwich counters.

LOOKING DOWNSTREAM

1/4" PILOT Y SCINTILLATOR

TO 56AVP PHOTOTUBES

1/2" LEAD
5/8" ALUMINUM

1/4" PILOT Y SCINTILLATOR

32"
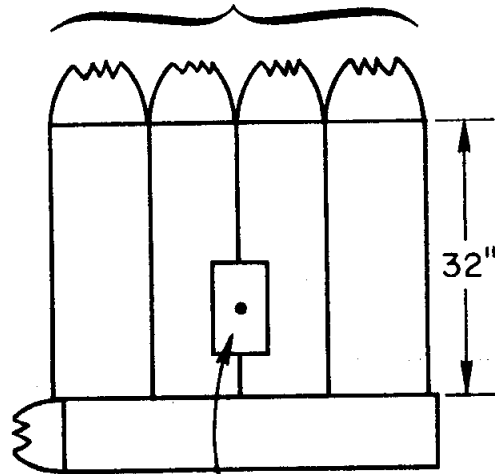
RECTANGULAR HOLE
FOR CHARGED PART-
ICLES AND BEAM
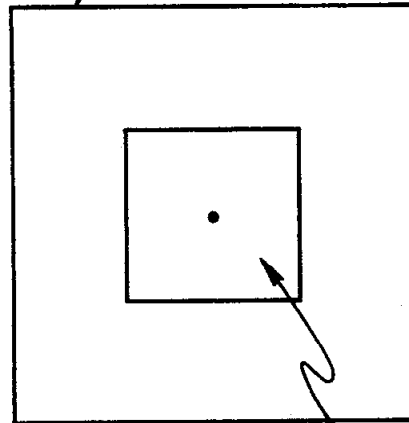
SQUARE HOLE FOR BEAM,
CHARGED PARTICLES, AND
PHOTONS

UPSTREAM COUNTER
PLANE

CENTER
CONVERTER PLATE
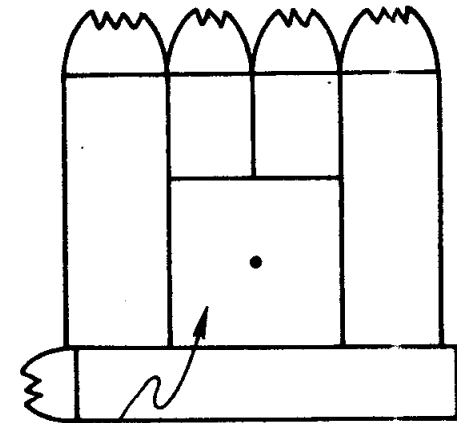
DOWNSTREAM
COUNTER PLANE

2134A10

FIG. 6--DV lead-scintillator sandwich veto counters.

H. Optics

The spark chambers were viewed directly by a 70 mm camera positioned 70' from the magnet and with a demagnification of 75. To obtain the third (depth) dimension each chamber was equipped with a stereo mirror view.

Fiducial marks (zenon flash tubes) were placed at the four corners of the magnet and were flashed for every picture. They were measured for every frame and defined the origin, tilt angle of the film in the camera, and magnification. Numerous other flashing fiducials were spread about but never used in the data analysis. In addition, each chamber was equipped with so-called dc fiducials which were turned on at the beginning of each roll for a few frames. These fiducials supplied a check of the mirror constants; no changes in the mirror orientation from the survey values were found except for a slight displacement of the T_1 mirror.

Pictures of straight through beam tracks allowed a check of any systematic shift of a chamber mirror; a small (≈ 1 mm) shift in the T_1 origin was found and corrected.

I. Electronics System

The electronics system served many functions: The number of beam particles incident on the target was counted; an event trigger was generated when the scintillation counter information matched a preset "trigger" pattern; and data was sent to the data box to be recorded on film and to an on-line PDP-8 for diagnostic use.

As discussed in Section B of this chapter, a good beam particle was defined by the combination $B_1 \cdot HD \cdot \overline{(A_1 A_2)}$; that is, a count from the B_1 and HD counters in coincidence and no count from the hole-veto counter $A_1 A_2$.

The information from the CT hodoscope (see Section D) was used to determine the multiplicity of charged particles upstream of the magnet. The technique used is illustrated in the logical diagram of Fig. 7. The signals from the 16 CT counters were sent to discriminators producing standardized -0.7 volt 12 nsec wide pulses. All the CT pulses were combined in an OR circuit and the resultant pulse, clipped to 7 nsec width by a discriminator, was used to select the interior 7 nsec of the 12 nsec CT pulses; this technique eliminated time jitter differences between CT counters.

The strobed pulses were then added in linear mixers; the height of the output pulse was directly proportional to the number of counters firing. A window discriminator selected signals with pulse height in a given range. For $\rho^{\pm}$ runs we used CT = 1 and for ρ^{O} runs CT = 2.

The RG and FG counter information was treated in a similar fashion to the CT. The multiplicity was determined with the same design circuit. For our $\rho^{\pm}$ data, we required (RG + FG) $\geq$ 2 and RG $\geq$ 1, and for the ρ^{O} data, RG $\geq$ 2, FG = 0.

The veto information from the TV, DV, and A_3 counters was combined with OR circuits. A master coincidence was finally formed with all the above information input. For the $\rho^{\pm}$ we required a beam particle upstream of the magnet, one and only one count from the CT (i.e., one $\pi^{\pm}$), at least one count from the RG counter (i.e., at least one $\pi^{\pm}$ downstream of the magnet), and at least one additional count from the RG or from the FG hodoscopes (at least one photon), and no veto firing. Symbolically, our trigger is written as $\left(B_1 \cdot HD \cdot (\overline{A_1 A_2}) \right) \cdot (CT = 1) \cdot (RG \geq 1) \cdot (RG + FG \geq 2) \cdot (\overline{TV + DV + A_3})$.

CT1

12 nsec
PULSE

CT16

OR

DISC

CLIPS TO
7 nsec PULSE

STROBE

STROBED COINC.

LINEAR MIXER

DISC

CT = N

SELECTS
PULSE HEIGHT
CORRESPONDING
TO N PULSES
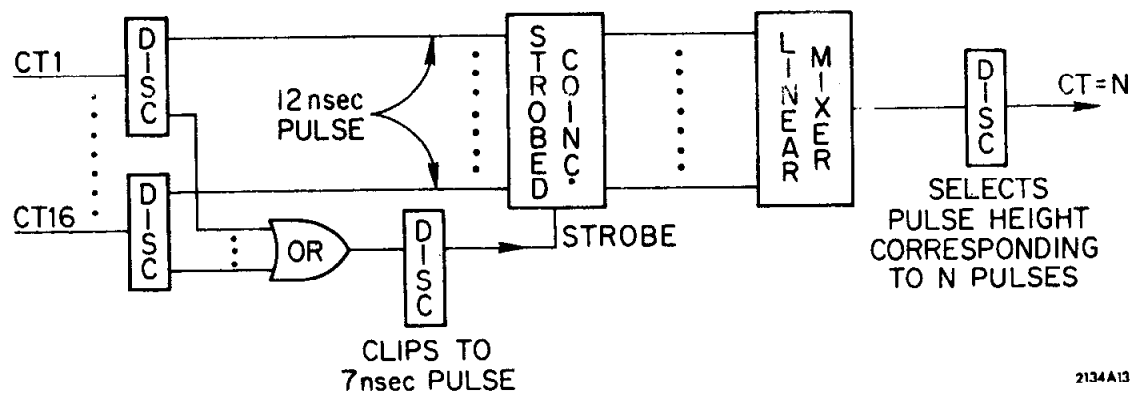
2134A13

FIG. 7--CT fast multiplicity counting circuit.

For the ρ^0 we required two charged particles upstream and two charged particles downstream of the magnet and no particles in the thick plate section of T_2. Symbolically this reads $(B_1 \cdot HD \cdot \overline{A_1 A_2}) \cdot (CT = 2) \cdot (RG \geq 2) \cdot \overline{(TV + DV + A_3 + FG)}$.

Once the trigger condition was met, a signal was sent to trigger the spark chambers. Also, the state of all of the counters was recorded via a latch system. This information was sent to the data box and to an on-line PDP-8. A counter that had fired was indicated on the data box - and on film - by a neon light. The roll and frame number was also displayed on the data box both with nixie tubes and with neon lights in BCD code.

We monitored accidental vetoes by forming $B \cdot \overline{V}_{del}$ where B is the beam signal and $\overline{V}_{del}$ means the veto signal out of time (delayed). This loss averaged around 8% and was corrected for roll by roll.

J.   Performance of the Apparatus

All counters were checked on cosmic rays before installation. The efficiency was invariably high. We use $100^{+0}_{-1}\%$ as the trigger counter efficiency. No anomalous effects in the data associated with an inefficient trigger counter were found.

The veto counters were also highly efficient on cosmic rays. In the experiment they were in regions populated by many low energy particles; thus it is not clear what to give for an efficiency. Inefficiencies in those counters will only result in more background pictures.

The spark chamber efficiency is a complicated function as it may depend on many variables. On single charged tracks the chambers are known to be $\approx 100\%$ efficient. To gain information about the chamber performance in the actual experimental condition we studied, for charged tracks, the distribution of the number of sparks measured per track. Chamber inefficiency losses occur when a track has too few sparks to be measured. For T_2, T_3, R_1, and R_2, the requirement was three or more to be measured; for T_2 we only required two or more. By this method we found our apparatus efficiency to detect a charged track was $100 \, {}^{+ \, 0}_{- \, 1}\%$.

The previous technique is not a useful way to determine the photon detection efficiency, for the dominant problem is one of finding the photons on a scan. We have no way, in this experiment, of calibrating absolutely the chamber photon detection efficiency. However, by studying the decays of the $K^{\pm}$ mesons in the beam we are able to determine the relative chamber, scanning, and measuring efficiency as a function of photon energy. This will be discussed in the next chapter. To summarize, we find no change in the T_3/T_4 chamber efficiencies over the photon energy range $200 \, \text{MeV} \leq E_{\gamma} \leq 13 \, \text{GeV}$. As the chamber detection efficiency should be very high for $E_{\gamma} = 13 \, \text{GeV}$ (showers here typically have ≥ 20 sparks) we will assume the chamber detection efficiency to detect both photons is $100 \, {}^{+ \, 0}_{- \, 5}\%$.

CHAPTER III

DATA REDUCTION AND EVENT SELECTION

A. Introduction

Our data consists of 66 rolls (3400 pictures/roll) of ρ^+ target full, nine ρ^+ target empty, 65 ρ^- target full, 10 ρ^- target empty, 6 1/2 ρ^0 target full, and one ρ^0 target empty roll. We also have some 8.0 GeV/c data but have not been able to analyze it because of poor beam quality and high backgrounds.

All the rolls were scanned and candidates for events sent to the measuring table; here the event was rescanned and, if still a potential good event, measured. Next, the real space positions of tracks were reconstructed from the film measurements. Our data contains four known types of events: elastic events, $K^{\pm}$ decay events, $\rho^{\pm}$ events, and ρ^0 events. Methods to identify each type of event were developed. In the $\rho^{\pm}$ case, this included a special scan of all the events to determine the relative photon energy; as explained in Chapter I, this was needed to resolve the π^0 ambiguity. The final results of this process were three sets of events, ρ^+, ρ^0, and ρ^-. Finally, the efficiency of this process, and of each substep, to find good events was determined.

B. Scanning

The film was first scanned by the SLAC Hummingbird flying spot digitizer which decoded the data box; the trigger counter information and the roll and frame number were obtained. Next, scanners of the SLAC CDA group examined the film; briefly they recorded the following information:

1. NRN

For the $\rho^{\pm}$ data the number of rear neutrals in T_3/T_4 was recorded.

A rear neutral was defined as a shower-like track beginning in the thick plate regions of T_3 or in the first or second gap of T_4 which pointed in a general way toward the target in both the direct and stereo views.

2. NRPI

For $\rho^{\pm}$ and ρ^0 data, the number of rear pions (charged tracks) was recorded. A rear pion consisted of three or more sparks laying on a straight line in the thin plates of T_3 which pointed generally toward the target in the stereo view (the magnet bends vertically) and made an angle to the nominal beam line (i.e., to the horizontal) of not more than 45°.

3. NFPI

The number of front pions was recorded. A front pion was defined as a track in both T_1 (two or more sparks) and in T_2 (three or more sparks with at least one in the first three gaps) which formed a straight line in the direct view pointing toward the hydrogen target.

4. NFN

For the $\rho^{\pm}$ data, the number of front neutrals was recorded. The scanners were requested to look for a front neutral only if a FG trigger counter had fired; as discussed later this was a mistake. A front neutral was a shower-like track appearing in the thick plate section of T_2 (i.e., not in the first three gaps) which pointed in the general direction of the target in both direct and stereo views.

5. NPRO

The number of proton tracks in R_1 and R_2 was recorded. While fairly broad classifications were used, we included in later analysis only those tracks appearing in both R_1 and R_2 pointing toward the target in the direct view.

The efficiency of the scan will be discussed at the end of this chapter.

C. Measuring

Potential events were sent to the measure table. The scan was verified by the measurer and the event measured on the SLAC NRI system.

For the $\rho^{\pm}$ data, we normally chose as ρ candidates, events with two, and only two, neutrals (NRN + NFN = 2) and with at least one charged particle in T_1, T_2, and T_3; this is in the spirit of the optical veto as discussed in Chapter I. However, we measured events with two or more neutrals for about 15 rolls of data. By selecting $K^{\pm}$ events in this sample (a 3-C fit) we were able to determine the event loss (accidental veto rate) when restricting ourselves to two neutral events; this will be discussed in detail in the next chapter.

For the ρ^o data, we measured all events with two or more charged particles both upstream and downstream of the magnet. By using the CT counter information we were able to throw out, with excellent (~ 10 nsec) time resolution, accidental tracks.

The measurers were asked to measure all the visible sparks on charged tracks, in both direct and stereo views, and three points, including the initial spark, along a neutral track (by using the first spark measurement we verified the neutral track did indeed start in the thick plate section of T_2 or T_3/T_4). The four main fiducials were also measured.

D. Geometrical Reconstruction

The measurement data and data box information were sent to the computer program LOCUS which performed the following tasks:

1. The fiducial measurements established the relation between the real space and film coordinates. Using the known mirror positions the

real space three dimensional coordinates were reconstructed from the NRI measurements of tracks.

2. Tracks in T_1 and T_2 were matched together by fitting straight lines simultaneously in direct and stereo views. The χ^2 distribution from these fits indicated a measuring and reconstruction accuracy per spark of 0.75 mm in real space.

3. The CT counter information was used to discard $T_1 T_2$ tracks not passing through an active counter.

4. Remaining $T_1 T_2$ tracks were extrapolated through the magnet in the stereo view (the magnet bends in the vertical) and matched with T_3 charged tracks. The direct view information was then used to determine the track's momentum. The momentum resolution of our system for a track with momentum P is (FWHM) $\delta P/P = 4\% \times P/(15.0\ \text{GeV/c})$. This number has been checked on 8.0 and 15.0 GeV/c beam tracks.

E. Selection of Elastic Events

The presence of elastic events in our $\rho^{\pm}$ data is seen as a sharp peak around 15.0 GeV/c in the $\pi^{\pm}$ momentum spectra. We remove elastic events by applying the $\pi^{\pm}$ momentum cut of 14.1 GeV/c; this removes no $\rho^{\pm}$ events. The presence of elastics may seem a bit strange as our trigger requires two or more counters downstream of the magnet and we require two neutral tracks to be seen on the scan. Elastically scattered pions frequently fire two RG counters by interacting in the thick plates of T_3; and accidental tracks and/or products from the thick plate interactions are occasionally perceived as neutrals.

F. Selection of $K^{\pm}$ Events

Our beam contained a small $K^{\pm}$ meson component. Our apparatus

accepted with high efficiency the $K^{\pm}$ decays in the region of the hydrogen target. We have about 2000 K^+ decays and 800 K^- decays. These K events have many uses, as we shall find, and must also be removed as a contamination to our $\rho^{\pm}$ events. We identify K events by the following procedure: the beam and charged pion four-momentum are known, hence we can reconstruct the missing mass which should be that of a π^o. Actually, we do a least-squares fitting procedure assuming the missing particle is a π^o (a 1-C fit). Potential K's are selected by a χ^2 cut. The π^o must be coplanar with the observed two photon plane: we make a coplanarity cut. Next we reconstruct the energies of the two photons. This process is straightforward and rather similar to the methods used to select $\rho^{\pm}$ events when the recoil proton is seen.

Fairly broad cuts are made when rejecting K events from our ρ data. When selecting K events for diagnostic purposes we use tighter cuts and, usually, restrict the decay region to the target area.

G. <u>Selection of ρ^o Events</u>

Our ρ^o trigger selects events $\pi^- p \to \pi^+ \pi^- X^o$. We measure the beam π^- and the final state π^+ and π^- four-momentum and consequently can determine the four-momentum of the X^o system. The X^o mass distribution is shown in Fig. 8a. The neutron peak is seen strongly with a long high mass tail with no clear structure. In particular no sign of the $\Delta^o(1238)$ nucleon resonance is seen; however, the mass resolution is inadequate to rule out the presence of a Δ^o signal completely. We have tried to enhance any Δ^o signal by selecting events with a $\pi^+ \pi^-$ mass in the ρ band $665 \leq m_{\pi\pi} \leq 865$ MeV. Figure 8b shows this distribution. Again there is no Δ^o seen.

Our Monte Carlo simulations indicate that the neutron mass distribution

$$\pi^-p \longrightarrow \pi^+\pi^-x^\circ$$

ALL EVENTS

$665 \leq M_{\pi\pi} \leq 865$ MeV

x° MASS (MeV)

EVENTS/100 MeV

2134A9
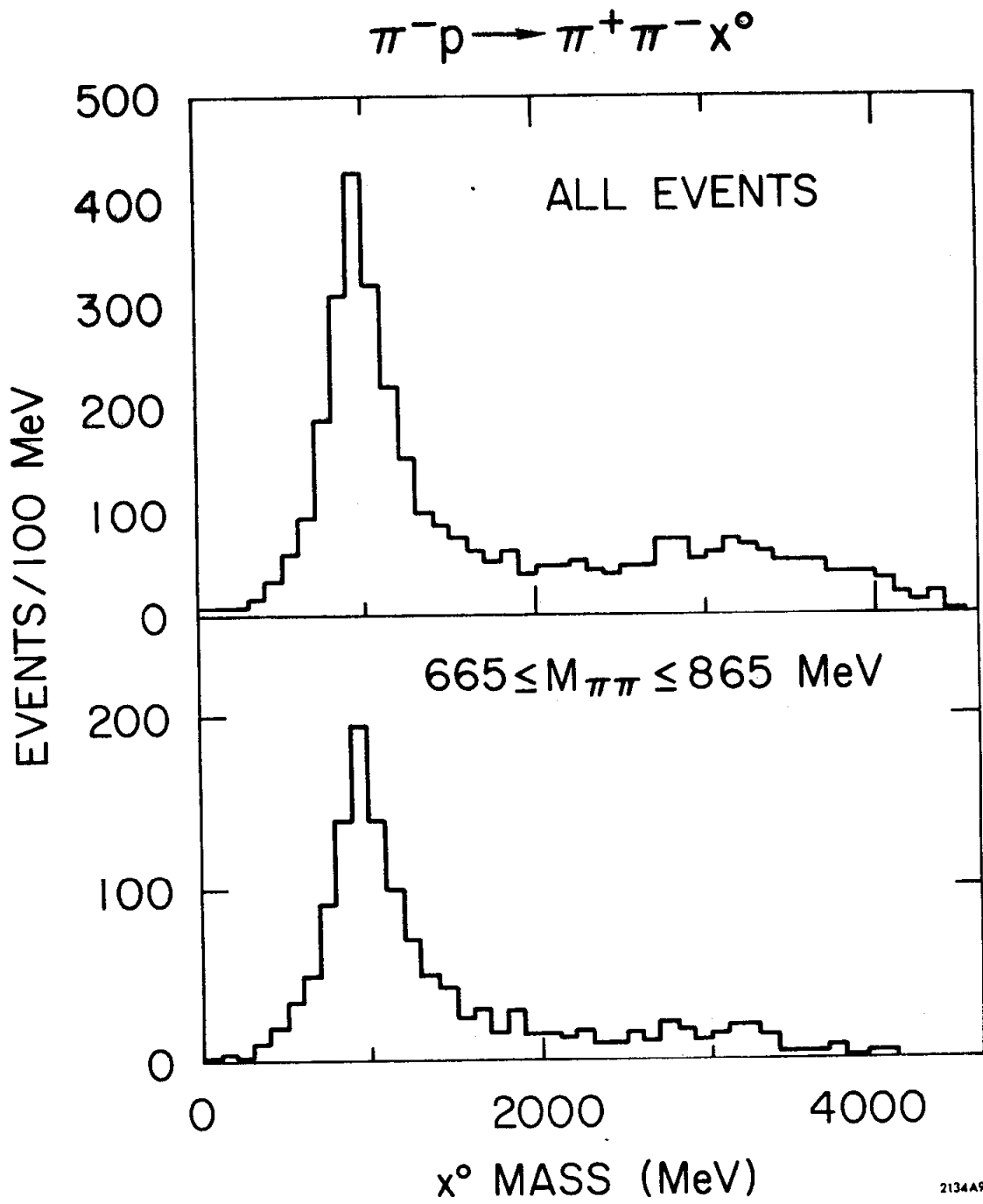
FIG. 8--Missing mass spectrum (M$_X$) for the reaction $\pi^-p \rightarrow \pi^+\pi^-$X, all events, and events with $665 \leq M_{\pi\pi} \leq 865$ MeV.

should be symmetric. We have used the low mass side of the neutron peak to subtract off the high mass side of the peak; again no Δ^o signal is seen. Finally we have restricted our data to symmetric $\pi^+ \pi^-$ decays where our missing mass resolution is sharpest and find no Δ^o signal. We estimate our Δ^o contamination to the ρ^o data to be $5 \pm 5\%$.

This result is reasonable even though the $\rho^o \Delta^o$ cross section is larger than the $\rho^o n$ cross section.[14] Even at $t \simeq t_{min}$ the Δ^o appears with about 50 MeV kinetic energy added to the Q value for the decay of about 160 MeV. The decay state is $2/3 \; \pi^o n$ and $1/3 \; \pi^- p$; our veto system is sensitive to both of these. Thus, we would expect to veto (and evidently do) Δ^o events with high efficiency.

Next we select $\pi^+ \pi^-$ events with the X^o mass cut. The X^o mass resolution is a function of the $\pi^+ \pi^-$ decay; for symmetric decays we choose events with the X^o mass within 300 MeV of the nominal neutron mass while for asymmetric decays we take events within 600 MeV of the neutron. These points correspond to a three standard deviation cut.

The ρ^o meson is clearly seen in the $\pi^+ \pi^- n$ mass distribution (Fig. 9). We select ρ^o events in the range $665 \leq m_{\pi\pi} \leq 865$ MeV; 817 events in the region $0 \leq |t| \leq 1.0 \; (\text{GeV/c})^2$ were found.

H. Selection of High-t $\rho^{\pm}$ Events

The high-t $\rho^{\pm}$ region is defined by $|t| \geq .08 \; (\text{GeV/c})^2$. In this region the recoil proton from good $\pi^{\pm} p \rightarrow \pi^{\pm} \pi^o p$ events must be visible in R_1 and R_2 or have been detected in the TV veto counters. Events with protons were kinematically analyzed with a program which shall be referred to as PROE. PROE selected visible proton events fitting the above reaction in the following way:
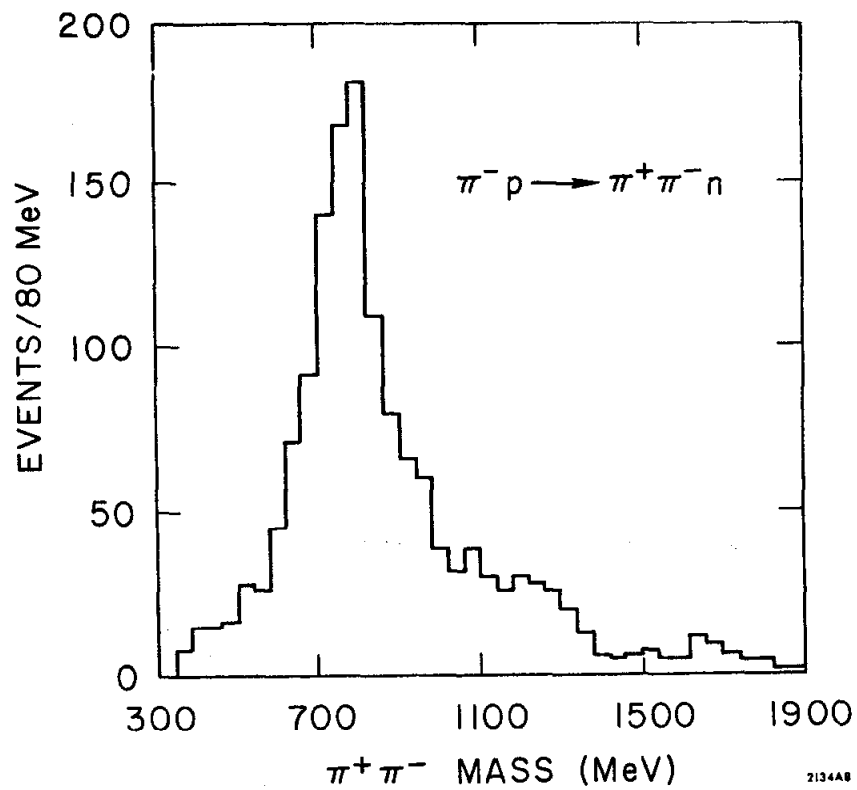
FIG. 9--Invariant mass spectrum ($M_{\pi\pi}$) for the reaction $\pi^- p \to \pi^+ \pi^- n$.

1. Only two neutral events were considered; the loss of good events due to accidental picture vetos will be determined in the next chapter.

2. There must be one and only one $\pi^{\pm}$ track passing through a firing or trigger counter.

3. There must be at least one recoil track.

4. All tracks must pass the fiducial cuts (See Section G).

5. $K^{\pm}$ and elastic events are rejected (Sections F and G).

6. The distance of closest approach between the $\pi^{\pm}$ and p is computed; Fig. 10a shows this distribution and our good vertex cut.

7. The interaction vertex must fall within the hydrogen target volume. Fig. 10b shows the vertex distribution along the beam and the target cut. Fig. 10c shows the transverse distance distribution and cut.

8. Four-momentum conservation is used to compute the recoil and each photon's momenta. The invariant photon-photon mass squared $m_{\gamma\gamma}^2$, is calculated and a π^0 mass cut made; Fig. 10e shows this. The recoil mass squared, m_r^2, is also calculated and a proton mass cut made as shown in Fig. 10d.

All high-t events must pass PROE. In addition we eliminated from our final sample events with one neutral in T_3 and one neutral in T_2. This was because of our belated realization that the low energy photons typical in T_2 did not necessarily fire the FG counters; our T_2 neutral scan was conditioned on a FG firing. Once we had decided not to use this data, we rejected all events with a FG firing. This, of course, will cause a slight accidental loss of good events which we shall determine in the next chapter.
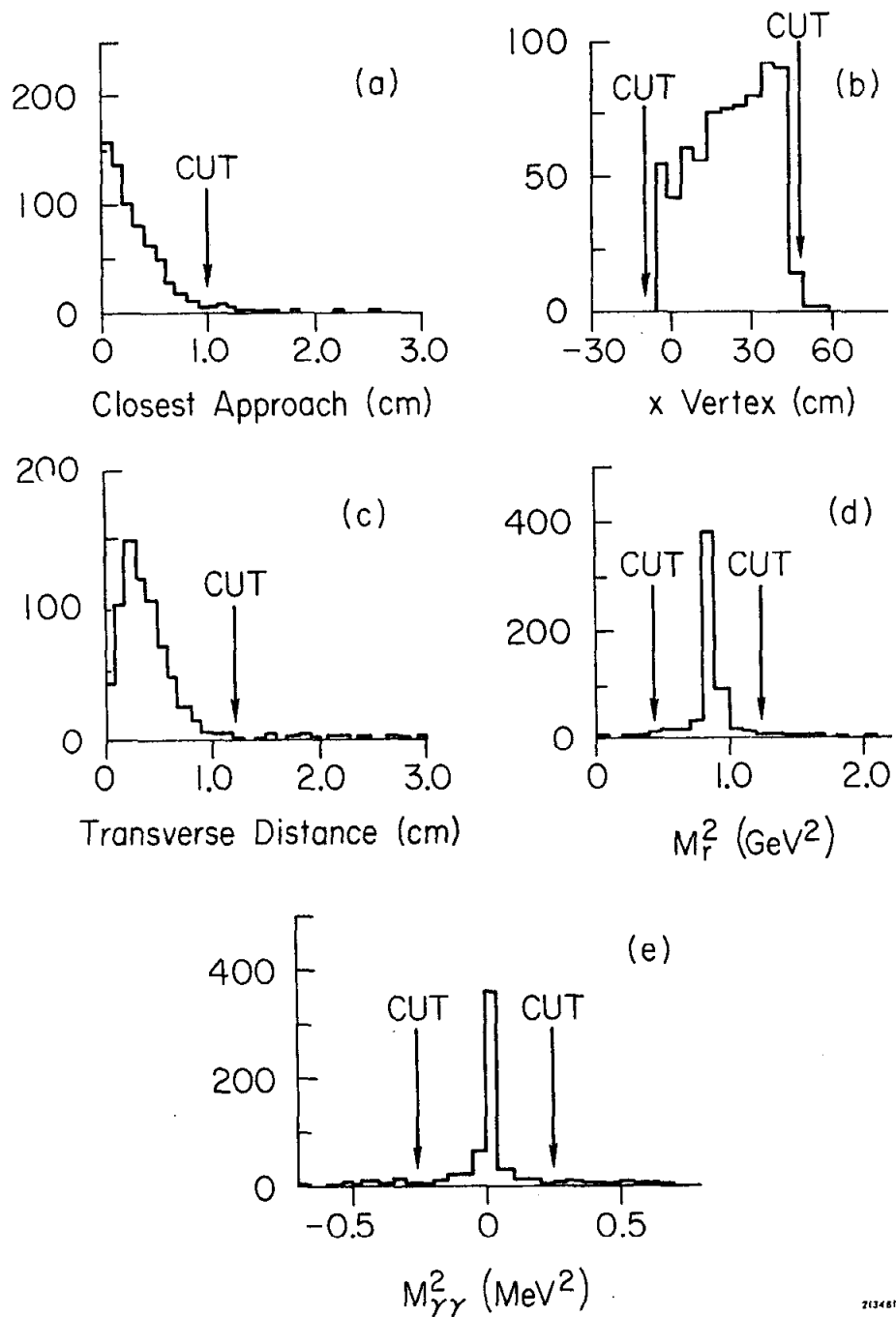
FIG. 10--Cuts made to select events belonging to the channel $\pi^{\pm}p \to \pi^{\pm}\pi^{0}p$ when the proton is detected: (a) Minimum distance of approach of the extrapolated $\pi^{\pm}$ and p tracks; (b, c) Vertex location within the target volume; (d) Mass of the recoil system is that of a proton; (e) Effective mass of the $\gamma\gamma$ system is that of a π^{0}.

Our final sample contained 146 15.0 GeV/c ρ^+ high-t events and 144 15.0 GeV/c ρ^- high-t events.

I.   Selection of Low-t $\rho^\pm$ Events

The low-t region is defined by $|t| \lesssim 0.08$ $(GeV/c)^2$. For $|t| \lesssim 0.03$ $(GeV/c)^2$ no protons are seen while for $0.03 \lesssim |t| \lesssim 0.08$ $(GeV/c)^2$ about 20% of the events will have protons. We are not able to separate the proton and no-proton region because of limited azimuthal angle resolution in this region; if there is a proton seen we use PROE, described in Section H, to select events. If no proton is seen we use a second program, NOPROE, to select events. However, before NOPROE can be used we must concern ourselves with the π^o ambiguity present when the proton is not observed.

In order for NOPROE to determine the unmeasured variables when the proton is not seen it must assume the recoil system is a proton and the two photons come from the decay of a π^o; and it must know how to match the particles in the hypothesis with the tracks observed in the experiment. Additional information must be supplied to tell it which gamma goes with which neutral track. Depending on the assignment made, it can obtain two kinematically different solutions; in 45% of the cases one or the other solution can be rejected because it has $|t| > 0.08$ $(GeV/c)^2$ which is not allowed since we have seen no recoil track. In the other 55% we determine which photon has the higher energy and so resolve the ambiguity.

All two neutral events were returned to the scan table. Three methods of relative energy determination were investigated: the number of sparks in each shower was counted; the length of each shower was measured (and if it went out the back of the chamber); a subjective estimate based on shower opening angle and spark brightness was made. All methods yielded similar

results. The method used for the balance of the data follows:

1. If both tracks stopped in the chamber the longer was assigned the higher energy.

2. If neither stopped in the chamber, the scanner's subjective estimate was used.

3. If only one stopped in the chamber it was considered the less energetic.

We are able to calibrate this method using the K decay events. In Fig. 11a we plot the energy discrimination accuracy as a function $\cos \Theta^*_{\pi^0}$ where $\Theta^*_{\pi^0}$ is the π^0 decay angle in the π^0 rest system. In Fig. 11b the ordinate is the photon energy difference.

We have made studies using Monte Carlo techniques to investigate the effects of the π^0 ambiguity on the physics variable for this experiment, t, $m_{\pi\pi}$, $\cos \Theta^*_{p}$, and ϕ^*_{ρ} ; we have found no systematic effects but a loss of resolution in these variables. In these studies we always used t to resolve the π^0 ambiguity if possible; otherwise we used various models for the energy discrimination scan. We have also included measuring errors and momentum errors in our simulation. Fig. 12 shows the results. The curves labelled (a) are computed assuming the scanner always makes the correct choice; in the high-t region, where there is no ambiguity, this is appropriate. The curves (b) assume the scanner always makes the wrong choice and are the worst case. The curves (c) simulate the real scanner.

Once the energy discrimination scan is available the program NOPROE is used on no-proton events to solve for the proton four-momentum and the two photon energies.

We then select low-t $\pi^{\pm} \pi^0 p$ events as follows:
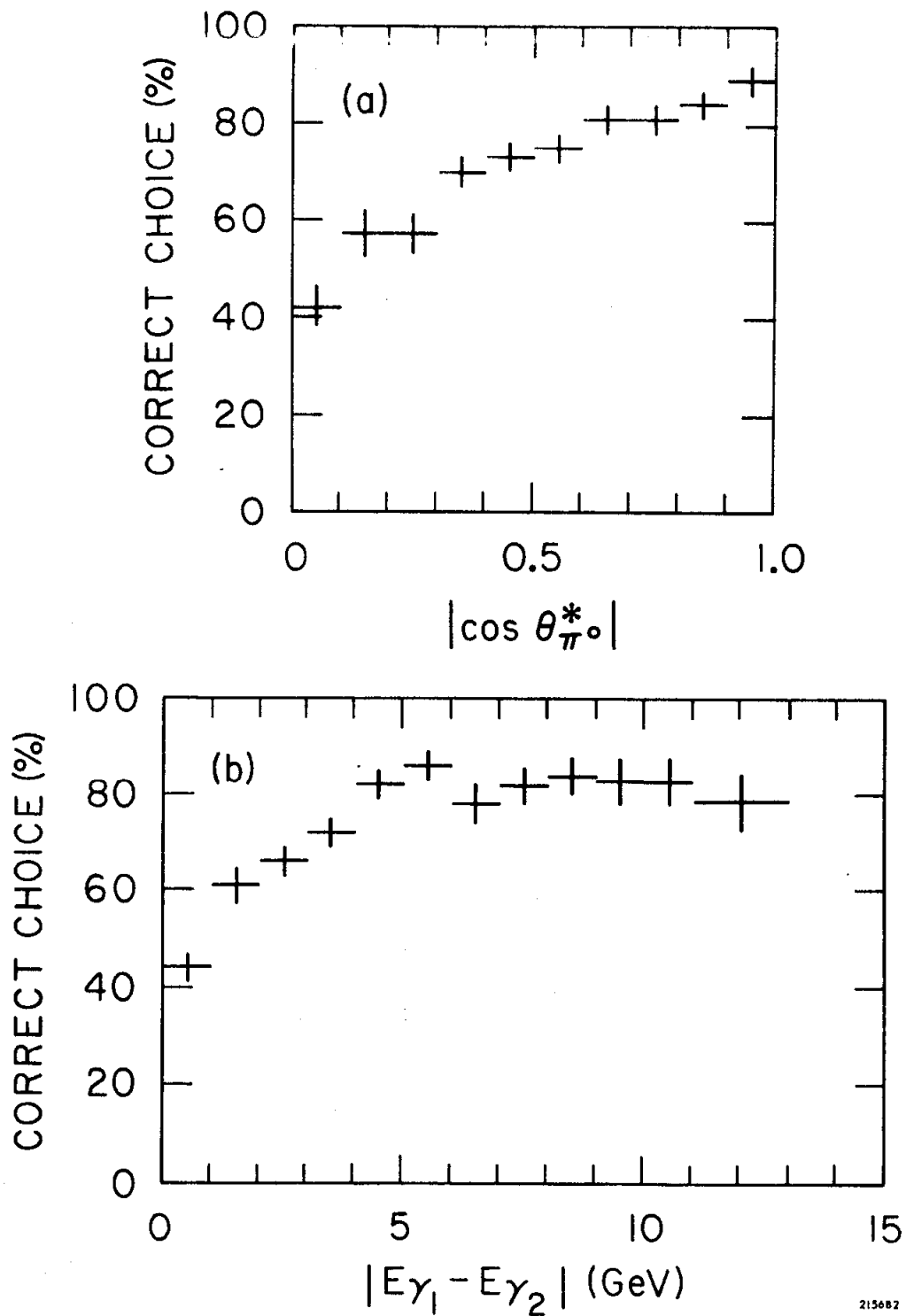
FIG. 11--The ability of scanners to correctly select from two γ-ray showers the one with more energy as a function of: (a) The π^0 rest frame decay angle; (b) The reconstructed energy difference between two photons.
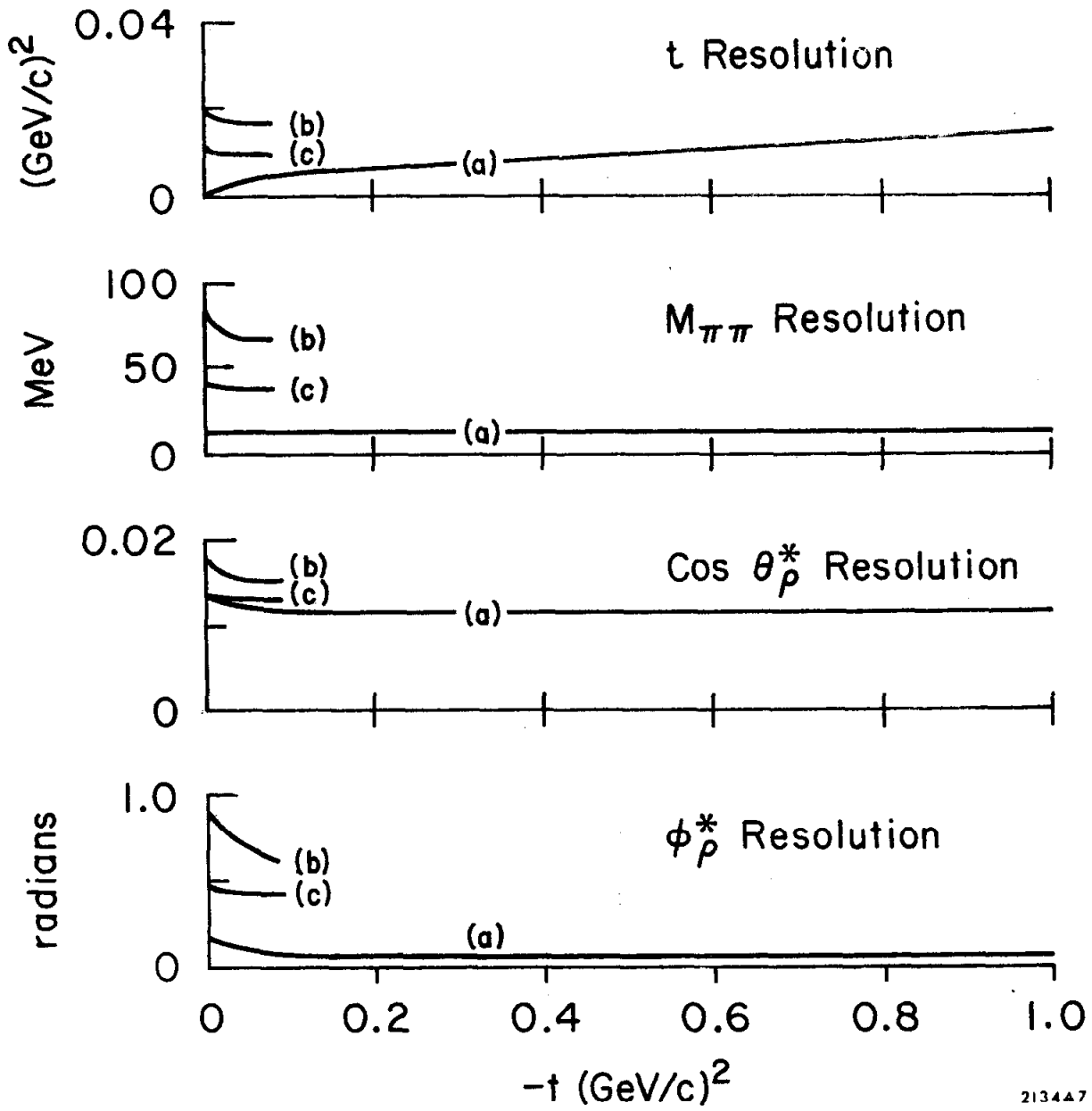
FIG. 12--Calculated resolutions as a function of momentum transfer. Curve (a) assumes there is no π^0 ambiguity; (b) assumes the scanner always makes the incorrect choice; (c) attempts to model the actual scanner based on the data in Fig. 11.

1. There must be two and only two neutral tracks; they must pass the fiducial cuts.

2. There must be exactly one $\pi^{\pm}$ track present; it must pass the fiducial cut.

3. K decay and elastic events are rejected.

4. If there is a track in R_1 and R_2 which makes a good vertex with the $\pi^{\pm}$ the event must belong to the channel $\pi^{\pm}p \rightarrow \pi^{\pm}\pi^{o}p$ as determined by PROE; if it passes PROE with $|t| < 0.08$ $(GeV/c)^2$ it is a good proton-visible low-t event (of course events passing PROE with $|t| > 0.08$ $(GeV/c)^2$ are high-t events). If the event fails PROE it is rejected; accidental picture veto losses will be determined in the next chapter.

5. If there is no good-vertex proton we require that the $\pi^{\pm}$ must intercept the hydrogen target at a point also intercepted by the beam (taking account of measuring uncertainties). The resultant vertex must lie in the target.

Events surviving these steps are called good low-t $\pi^{\pm}\pi^{o}p$ events. Fig. 13 shows the $\pi^{+}\pi^{o}$ and $\pi^{-}\pi^{o}$ mass distribution of the low-t and high-t events. The ρ meson in each case is very clearly seen. The $K^{\pm}$ mesons have been subtracted in these plots. A vestige of the K^{+} can be seen in the ρ^{+} data; we are subtracting about 1400 K^{+} events so it is not surprising that a few remain.

We select our final ρ^{+} and ρ^{-} samples by combining the low-t and high-t events and making the mass cut $665 \leq m \leq 865$ MeV. We have finally 811 ρ^{+} events and 778 ρ^{-} events.

J. <u>Data Reduction and Event Selection Efficiency</u>

The procedures described in this chapter were designed to detect, process, and finally produce all good ρ events for analysis. However, events
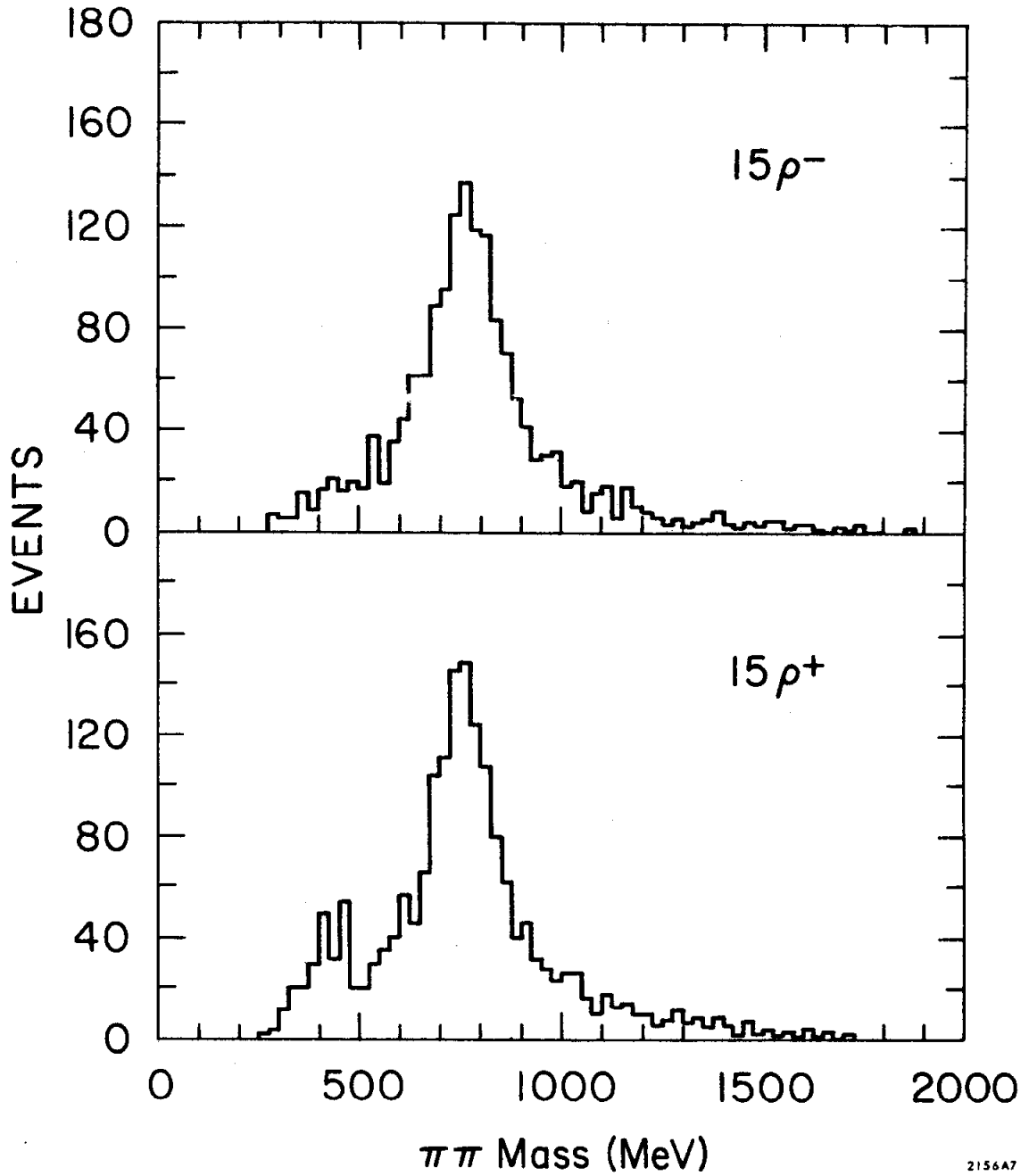
FIG. 13--The $\pi^+\pi^0$ and $\pi^-\pi^0$ invariant mass distribution for the reaction $\pi^\pm p \rightarrow \pi^\pm \pi^0 p$.

were occasionally lost, either in the scanning and measuring step or by subsequent failure to pass the various cuts.

We considered several ways to deal with this problem. We could have put all our film through the process again and again until all events were found, but this approach was considered impractical. Instead we chose to reprocess a sample of the data and, by comparison with the initial pass, attempt to understand our efficiency function. We sent through the data analysis system for the second time eight rolls of ρ^+, eight rolls of ρ^-, and one half each of two different rolls of ρ^0.

It is important to understand any correlations between the data analysis process efficiency and the physics variable of the experiment; we may, for example, expect a loss for $\rho^\pm$ events when $\cos \Theta_\rho \sim 1$ for this corresponds to low energy photons which may be more difficult for the scanner to detect. Or, we may expect a loss of events in the high-t region because a visible proton must be measured.

Let P_1 denote the original pass and P_2 the extra pass. Let the data be divided into N_k kinematical regions such that within the ith region there is a uniform efficiency ϵ^i per pass to detect an event; for example, we may divide the data into low-t and high-t regions and further subdivide the data by photon energy. Within each region we must make the statistical assumption that each event has an equal chance of being detected by the data analysis process.

Let N_1^i be the number of events in the ith region detected on P_1 and N_2^i the number detected on the second pass, and N_{12}^i the number detected on both passes. The best estimate of the efficiency from this data is

$$\epsilon^i = \frac{2N_{12}^i}{N_1^i + N_2^i}$$

with statistical error

$$\sigma_\epsilon^i = \sqrt{\frac{\epsilon^i(2 - \epsilon^i)(1 - \epsilon^i)}{N_1^i + N_2^i}}$$

The ρ^0 data was analyzed in this way. No systematic biases were found and we obtained the efficiency for the data analysis step of

$$\epsilon_{\pi^+\pi^-}^{DA} = .77 \pm .05$$

We have divided our $\rho^\pm$ data into low-t and high-t regions and into low photon energy and high photon energy regions. We have also looked for inefficiencies associated with proximity of the spark chamber tracks to the beam areas which were deadened with mylar patches which sometimes flared. The only effect discovered is a low-t/high-t difference. We thus give our results in terms of a data analysis efficiency to detect a π and two photons, $\epsilon_{\pi\gamma\gamma}^{DA}$, and an efficiency to detect a proton, ϵ_p^{DA}. We find, combining the ρ^+ and ρ^- data, which within statistics are identical, that

$$\epsilon_{\pi\gamma\gamma}^{DA} = .73 \pm .02$$

$$\epsilon_p^{DA} = .84 \pm .05$$

We have determined the loss rate within each substep of the data analysis procedure and find, for the low-t data:

1. Scanning: $\approx 12\%$ of the good events are lost here.

2. Measuring: $\approx 4\%$ of the good events are lost here.

3. Geometrical reconstruction: $\approx 6\%$ lost here; this step catches most measurer errors.

4. Event selection: $\approx 4\%$ lost here; this step is sensitive to measurer accuracy.

Finally, we emphasize these efficiencies are for the data analysis step only and do not include apparatus inefficiencies. We have argued in the last chapter that the apparatus efficiency to detect charged particles is high, consistent with 100%. We have just concluded that the data analysis efficiency is uniform in the photon energy. By using the $K^{\pm}$ decay events we can investigate the combined apparatus and data analysis detection efficiency. We have simulated $K^{\pm}$ events, including the apparatus acceptance assuming 100% photon acceptance in T_3/T_4; these events have been binned according to the energy of the softer photon. The data has also been binned and a ratio of the data to prediction formed. Fig. 14 shows the result. The normalization is arbitrary, but no loss in efficiency is seen for low photon energy.
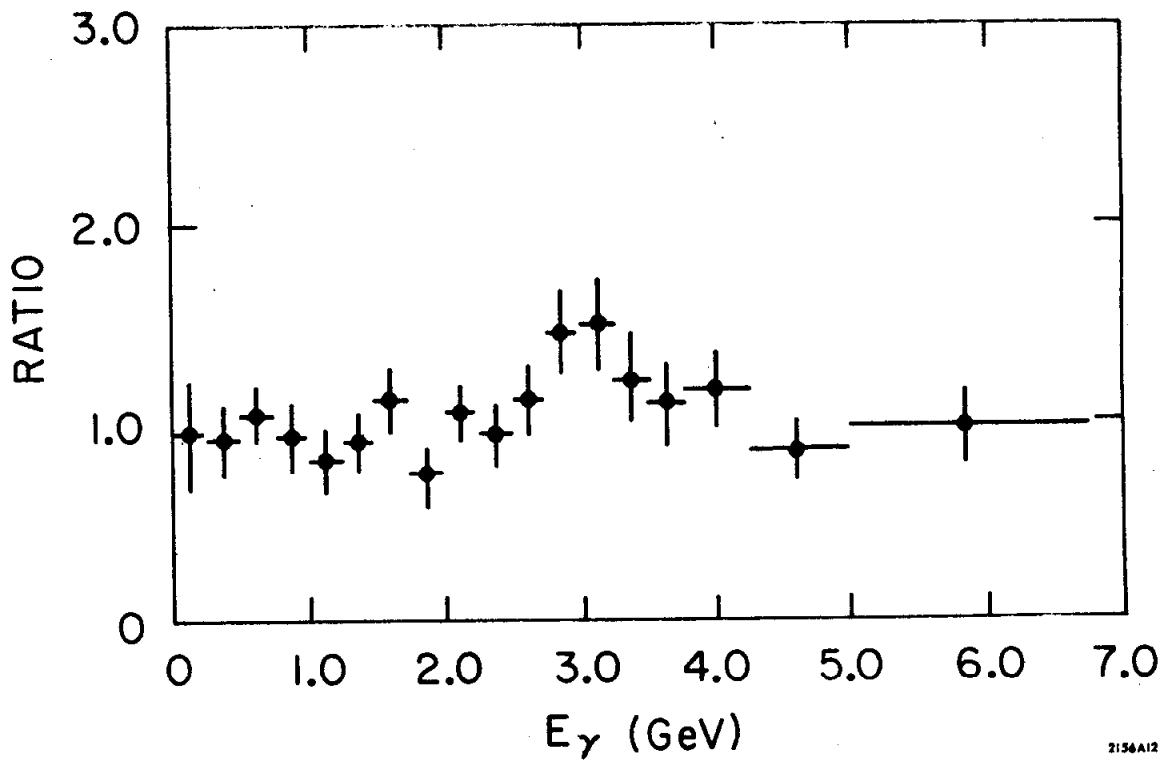
FIG. 14--Ratio of expected to observed number of photons for $K^{\pm} \rightarrow \pi^{\pm}\pi^{0}$ events as a function of the photon energy; the overall normalization is arbitrary.

CHAPTER IV

EXTRACTION OF ρ CROSS SECTIONS AND DENSITY MATRICES

A. Introduction

In this chapter the extraction of the cross sections and density matrix

elements from our raw ρ^+, ρ^o, and ρ^- data is discussed. Using a maximum

likelihood method we fit for dN/dt, the unnormalized cross section, and

$\rho_{mm'}$, the density matrix elements, taking into account the acceptance of

the apparatus. dN/dt is corrected for known losses. Non-ρ $\pi\pi$ backgrounds

are subtracted. Estimates of contaminations from other channels are made

and appropriate subtractions performed. The ρ cross sections and density

matrix elements are presented and the systematic errors are estimated.

B. Extraction of dN/dt and $\rho_{mm'}^{H}$

Our raw data consists of events selected by methods described in the

previous chapter and with the cut $665 \leq M_{\pi\pi} \leq 865$ MeV. If the apparatus

detection efficiency is perfect, dN/dt is extracted by counting the number

of events in a t bin, and $\rho_{mm'}$ by studying the $\pi\pi$ rest frame angular dis-

tribution. However, when the detection efficiency is finite and a function

of the physics variables of the experiment, the problem is more difficult

and, in the extreme case of zero detection efficiency in some regions

(generally the case in practical experiments), one must make assumptions

about the underlying angular distributions to proceed at all.

We assume only $\ell = 0$ and $\ell = 1$ partial waves are present in the $\pi\pi$

angular distributions. This provides a completely adequate description

of our data; a high statistics 15.0 GeV/c ρ^o experiment has also found this

to be true[15]. We also assume parity conservation which in any $\pi\pi$ rest

frame coordinate system with the y-axis perpendicular to the ρ scattering plane takes the form[16] $\rho_{mm'} = (-1)^{m-m'} \rho_{-m, -m'}$. Under this assumption the most general $\pi\pi$ angular distribution is:

$$W(\cos \Theta_\rho^*, \varphi_\rho^*) = \frac{1}{4\pi} \left[\frac{3}{2} \sin^2 \Theta_\rho^* + \frac{3}{2}(\rho_{00} + \frac{1}{3}\rho_s)(3 \cos^2 \Theta_\rho^* - 1) \right.$$

$$- 3\sqrt{2} \; \text{Re} \, \rho_{10} \sin 2\Theta_\rho^* \cos \varphi_\rho^* - 3\rho_{1,-1} \sin^2 \Theta_\rho^* \cos 2\varphi_\rho^*$$

$$\left. + 2\sqrt{3} \; \text{Re} \, \rho_{0s} \cos \Theta_\rho^* - 2\sqrt{6} \; \text{Re} \, \rho_{1s} \sin \Theta_\rho^* \cos \varphi_\rho^* \right] \qquad (4.1)$$

We have not, as of yet, specified the orientation of the z-axis within the ρ scattering plane. The helicity frame orientates the z-axis opposite to the recoil nucleon direction as viewed in the $\pi\pi$ rest frame. The Gottfried-Jackson frame is specified with the z-axis in the direction of the beam as viewed in the $\pi\pi$ rest frame; this frame is popular when a π is exchanged[17]. Here, though, the helicity frame is more appropriate and will be used exclusively.

The density matrix is a matrix of probability. In Eq. (4.1) the normalization

$$\rho_{00} + 2\rho_{11} + \rho_s = 1 \qquad (4.2)$$

has been used. We shall ultimately subtract ρ_s and renormalize for our study of the ρ meson. Notice that we do not determine ρ_s from the $\pi\pi$ angular distribution but only the combination $\rho_{00} + \frac{1}{3}\rho_s$. Section D of this chapter will deal with the determination of ρ_s. Also, we do not measure $\text{Im} \, \rho_{10}$, $\text{Im} \, \rho_{s0}$, and $\text{Im} \, \rho_{s1}$ because of parity invariance.

The actual technique used to estimate dN/dt and $\rho_{mm'}$ follows:
We first place our data, with the mass cut $665 \leq M_{\pi\pi} \leq 865$ MeV, in bins in t. Within a t-bin of width Δt, we subdivide the data into bins in $\cos \Theta_\rho^*$

and φ_ρ^* such that n_{ij}^t is the number of observed events in the ith $\cos \Theta_\rho^*$ and j^{th} φ_ρ^* bin.

We now make a prediction $\bar{N}_{ij}^t$ for this bin. Let $D(M_{\pi\pi})$ represent a Breit-Wigner mass distribution and $\epsilon(t, M_{\pi\pi}, \cos \Theta_\rho^*, \varphi_\rho^*)$ the apparatus detection efficiency. Then

$$\bar{N}_{ij}^t = \frac{\left(\frac{dN}{dt}\right) \Delta t \int_{665}^{865} D(M_{\pi\pi}) dM_{\pi\pi} \int_{ij^{th}\ Bin} d(\cos \Theta_\rho^*) d\varphi_\rho^* W(\cos \Theta_\rho^*, \varphi_\rho^*) \epsilon(t, M_{\pi\pi}, \cos \Theta_\rho^*, \varphi_\rho^*)}{\int_{665}^{865} D(M_{\pi\pi}) dM_{\pi\pi}}$$

We then minimize $-\ln L$ with respect to dN/dt and $\rho_{mm'}$, where the likelihood function is defined as

$$L = \prod_{ij} \frac{\bar{N}_{ij}^t {}^{n_{ij}^t}}{n_{ij}^t!} e^{-\bar{N}_{ij}^t} .$$

The errors in dN/dt and $\rho_{mm'}$ are defined as the increment necessary to increase $-\ln L$ by 0.5 while maintaining a minimum in all other variables.

The acceptance function $\epsilon(t, M_{\pi\pi}, \cos \Theta_\rho^*, \varphi_\rho^*)$ has been calculated with a Monte Carlo program which determines if a specified event is detected by the apparatus and then integrates over the interaction vertex location, the production azimuthal angle, and the π^0 decay. We show in Fig. 15a and Fig 15b the calculated $\rho^\pm$ acceptance as a function of $\cos \Theta_\rho^*$ and φ_ρ^* with $M_{\pi\pi} = 765$ MeV and $t = -.01$ $(GeV/c)^2$. Also, we show in Fig. 15c and Fig. 15d the dependence of ϵ on t and $M_{\pi\pi}$ assuming an isotropic decay distribution $(\rho_{00} + \frac{1}{3} \rho_s = \frac{1}{3})$. The most significant feature is the decreasing acceptance as $\cos \Theta_\rho^* \to \pm 1$. This limit corresponds to asymmetric ρ decays; the low acceptance results from high energy $\pi^\pm$ mesons being

- 46 -
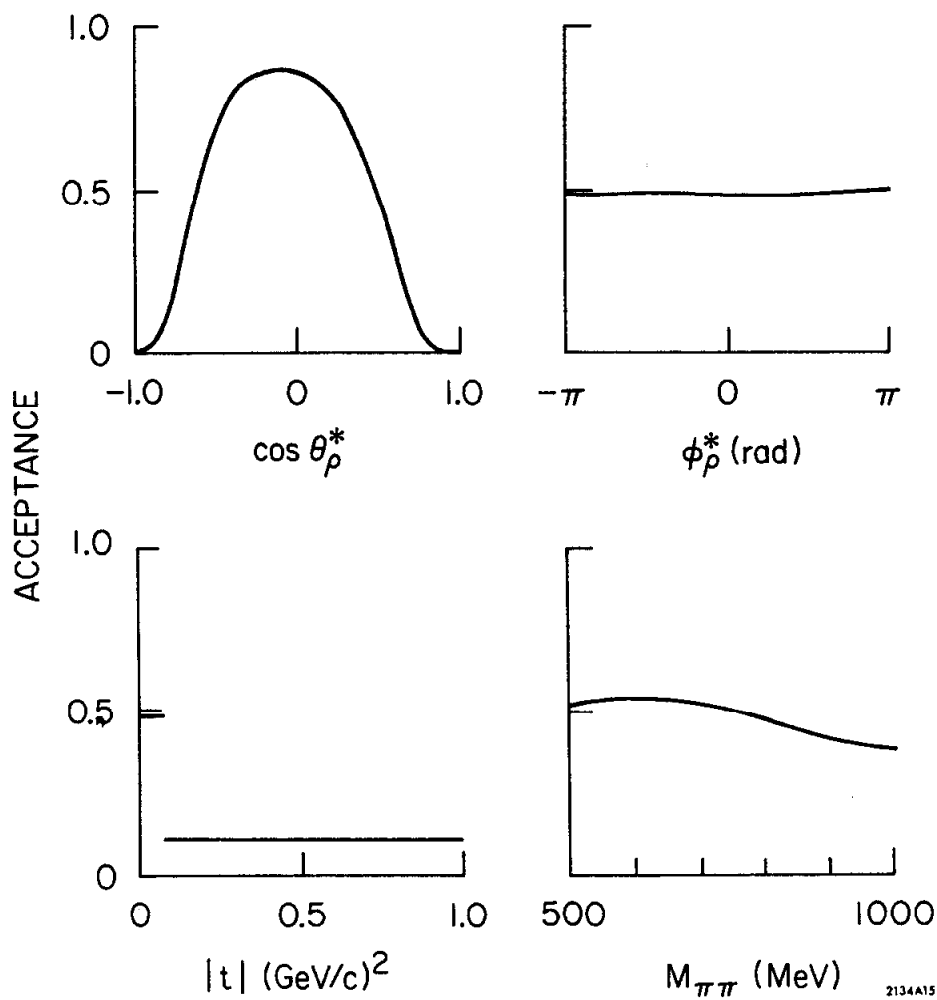
FIG. 15--The apparatus acceptance as a function of the "physics variables." The cos θ_ρ^* and φ_ρ^* distributions assume $t=-.01$ (GeV/c)^2 and $M_{\pi\pi}=765$ MeV. The t and $M_{\pi\pi}$ distributions assume isotropic distributions in cos θ_ρ^* and φ_ρ^*.

lost in the deadened beam areas of the spark chambers, low energy $\pi^{\pm}$ mesons being swept out by the magnet, and photons from a low energy π^o missing the chambers.

In Fig. 16 the modification of an underlying angular distribution by our acceptance function is illustrated for low-t ρ^+ data. The curve is the underlying distribution; the observed events are histogramed.

C.   Correction for Experimental Event Losses

In this section all known possible sources of event losses are tabulated.

1.   Events Vetoed by Knock-on Electrons.

Here we are concerned only with the case of a knock-on electron from a charged particle associated with the event in question firing a veto. Purely accidental vetoes, no matter what the source, are dealt with in item (3). Moving perpendicular to the beam line a knock-on electron had to penetrate 1 cm of hydrogen (on the average), .15" of aluminum, .05" of lead, and exceed the counter threshold to fire a TV. Of course, higher energy knock-ons do not move perpendicular to the beam line and so must penetrate a correspondingly greater thickness. Quantitatively we calculate a negligible probability for such a veto.

2.   Neutron Vetoes

This applies to ρ^o events and refers to vetoes in the TV counters from the recoil neutron. We have estimated this correction in a simple way, but, because of our lack of knowledge of counter thresholds, can not determine it accurately. Table 1 shows the results and the estimated systematic errors.
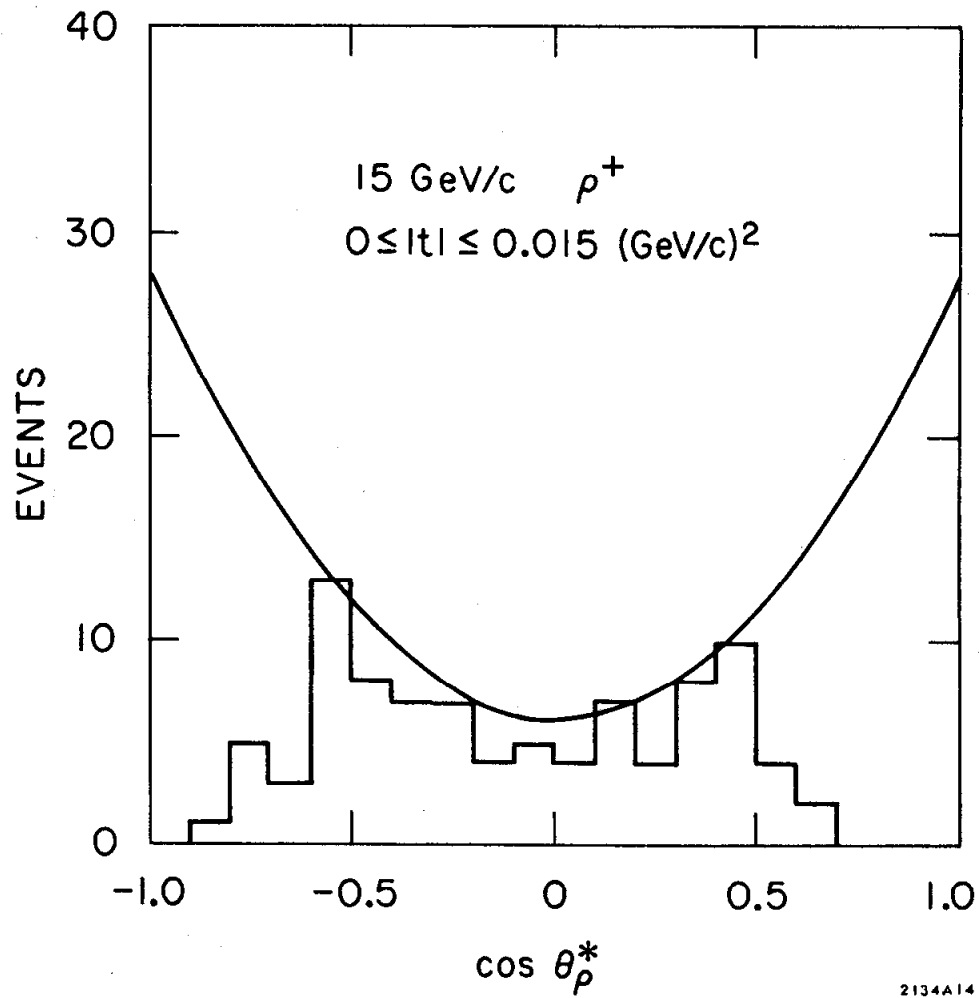
FIG. 16--Comparison of the angular distribution of observed events
(histogrammed) and the underlying distribution obtained
when the apparatus acceptance is removed (solid curve).

TABLE 1

ESTIMATED ρ^0 EVENT LOSS FROM NEUTRON VETOES

t BIN	EVENT LOSS
.000 -- .015	$7 \pm 5\%$
.015 -- .030	$7 \pm 5\%$
.030 -- .045	$6 \pm 5\%$
.045 -- .060	$5 \pm 4\%$
.060 -- .080	$4 \pm 4\%$
.080 -- .12	$3 \pm 3\%$
.12 -- .20	$2 \pm 2\%$
.30 -- .35	$1 \pm 1\%$
.35 -- .60	$1 \pm 1\%$
.60 -- 1.0	$1 \pm 1\%$

3.   Accidental Electronic Vetoes

This source of lost events was discussed in Section I of Chapter II; on the average about 8% of our events were lost from accidental vetoes. The statistical error in this correction is negligible; our estimate of the systematic uncertainly is $\pm$ 0.5%.

4.   Apparatus Detection Efficiency

This was covered in Section J of Chapter II. We found

$$\epsilon = 1.0 \, ^{+.00}_{-.05} \quad \rho^{\pm} \text{ events}$$

$$\epsilon = 1.0 \, ^{+.00}_{-.02} \quad \rho^{0} \text{ events}$$

These errors are our estimate of the systematic uncertainty.

5. Absorption of Initial and Final State Particles

Here we refer to the loss of events through secondary interactions with various elements of the apparatus. We have studied this loss by Monte Carlo simulations. For each t-bin we used the observed ρ angular distribution; the path length in the hydrogen target was computed and found to be, on the average, 25 cm for the beam particle, 14 cm for each secondary π, and 15 cm for each photon. We also looked at the loss rate as a function of the $\pi\pi$ decay angles and found, when all secondary particles were included, only a weak dependence. We thus make only an overall correction as shown in Table 2; our estimate of the systematic uncertainty is included.

6. Loss of Events by π Decay

To first approximation the decay $\pi \rightarrow \mu + \nu$ changes only the track momentum. As $M_{\pi\pi}$ and t depend only weakly on the $\pi^{\pm}$ momentum, we suffer no loss of events in the low-t $\rho^{\pm}$ regions. In the high-t and in the ρ^{o} regions a loss of events will occur because the recoil mass is altered sufficiently to fail the proton or neutron cut. We have estimated this and find losses of

$$0 \qquad\qquad \text{low-t } \rho^{\pm}$$

$$1 \pm 0.5\% \qquad\qquad \text{high-t } \rho^{\pm}$$

$$1 \pm 0.5\% \qquad\qquad \rho^{o}$$

The estimated systematic uncertainty is shown.

7. Data Analysis Efficiency

Chapter III was entirely devoted to the data analysis process and the last section to its efficiency. We found

$$\epsilon_{DA} = .73 \pm .02 \qquad \text{low-t } \rho^{\pm}$$

$$\epsilon_{DA} = .61 \pm .05 \qquad \text{high-t } \rho^{\pm}$$

$$\epsilon_{DA} = .77 \pm .05 \qquad \rho^{o}$$

TABLE 2

APPARATUS ABSORPTION LOSSES

Type of Absorption	Data Point	Loss
Beam in Target	$\rho^{\pm}$	$2.5 \pm 0.5\%$
	ρ^{o}	$2.5 \pm 0.5\%$
Final State Hadrons in Target	$\rho^{\pm}$	$1.5 \pm 0.3\%$
	ρ^{o}	$3.0 \pm 0.6\%$
Photons in Target	$\rho^{\pm}$	$2.6 \pm 0.5\%$
	ρ^{o}	---
Final State Hadrons in Chambers and Counters	$\rho^{\pm}$	$0.5 \pm 0.1\%$
	ρ^{o}	$1.0 \pm 0.2\%$
Photons in Chambers and Counters	$\rho^{\pm}$	$5.0 \pm 1.0\%$
	ρ^{o}	---
Total	$\rho^{\pm}$	$11.5 \pm 2.0\%$
	ρ^{o}	$6.5 \pm 1.0\%$

The errors shown here are _statistical._ In addition, we estimate there is an overall _systematic_ uncertainty of 5% in this correction.

8.   Picture Veto Loss: Neutrals

We rejected $\rho^{\pm}$ events with more than two neutral tracks found on the scan. Occasionally, a good event was accidentally rejected. By using our sample of events with more than two neutrals and identifying $K^{\pm}$ mesons we measured this loss rate to be 8% for $\rho^{\pm}$ events with a _statistical_ error of 3%. We estimate a negligible _systematic_ error.

9.   Picture Veto Loss: π

We rejected $\rho^{\pm}$ events with a second charged track in the π spectrom-meter which survived the CT cut. The accidental veto rate was $1.9 \pm 0.5\%$, with an estimated negligible _systematic_ error.

10.   Picture Veto Loss: Recoil

We rejected $\rho^{\pm}$ events with a recoil track in R_1 and R_2 which made an acceptable vertex with the π track but did not have an acceptable $\rho^{\pm}$ fit. The accidental veto loss as determined from $K^{\pm}$ decay events was $0.6 \pm 0.2\%$, with an estimated negligible _systematic_ error.

11.   Accidental Veto Loss: FG Veto

We ultimately did not use the data with neutrals in T_2. We then rejected all events with a FG counter firing. This introduces an accidental veto rate which was found from the $K^{\pm}$ decay events to be $1.1 \pm 3\%$ with an estimated negligible _systematic_ error.

12.   Failure to Convert a Photon

In scanning for events we required both photons to convert before the third gap of T_4. The probability of this is 99.6% and is a neglibible correction.

D.   Backgrounds and Contaminations

In this experiment we are concerned with the states $\rho^{\pm}p$ and $\rho^{o}n$ but

- 53 -

detect the states $\pi^{\pm}\pi^{o}p$ and $\pi^{+}\pi^{-}n$. The existence of a $\rho^{\pm}$ or ρ^{o} in the intermediate state must be inferred from the $\pi\pi$ invariant mass and from the $\pi\pi$ angular distribution. We term as <u>backgrounds</u> events belonging to the channel $\pi\pi N$ but not having a ρ in the intermediate state. Also our data (particularly our low-t $\rho^{\pm}$) may have <u>contaminations</u> from other (higher multiplicity) channels which are misidentified as belonging to the channel $\pi\pi N$.

In addition to the two usual sources of information about this problem - the $\pi\pi$ invariant mass and angular distributions - we have a third way of studying the low-t $\rho^{\pm}$ contaminations. In the high-t region we can use the proton recoil angle measurement to isolate a sample of high-t contamination events; this sample can then be extrapolated into the low-t region.

To begin, we consider the $\pi\pi$ mass distributions which are given in Fig. 9 and Fig. 13; these show clearly dominant ρ peaks with some flat background and contaminations. We have fit to these distrbutions, for various ranges of t, a relativistic Breit-Wigner [18] ($M_\rho = 765$ MeV, $\Gamma_\rho = 160$ MeV) plus a phase space background [19]. The $\pi\pi$ mass-dependent acceptance function has been included in this fit assuming the non-ρ events to be in a s-wave. Table 3 lists the results of this fit; the errors shown are statistical. A typical fit is shown in Fig. 17, in this case, the high-t ρ^{+} data. The ρ^{+} and ρ^{-} results are, within statistics, equal; in subsequent calculations the average will be used.

The $\pi\pi$ mass fits only measure backgrounds and contaminations which are "flat" in $M_{\pi\pi}$ relative to the ρ. A contamination to the low-t $\rho^{\pm}$ data which would exhibit a ρ mass structure could come, for example, from the channel $\pi^{\pm} + p \rightarrow \rho^{\pm} + \Delta^{+}$ where our veto system failed to detect the Δ^{+}.
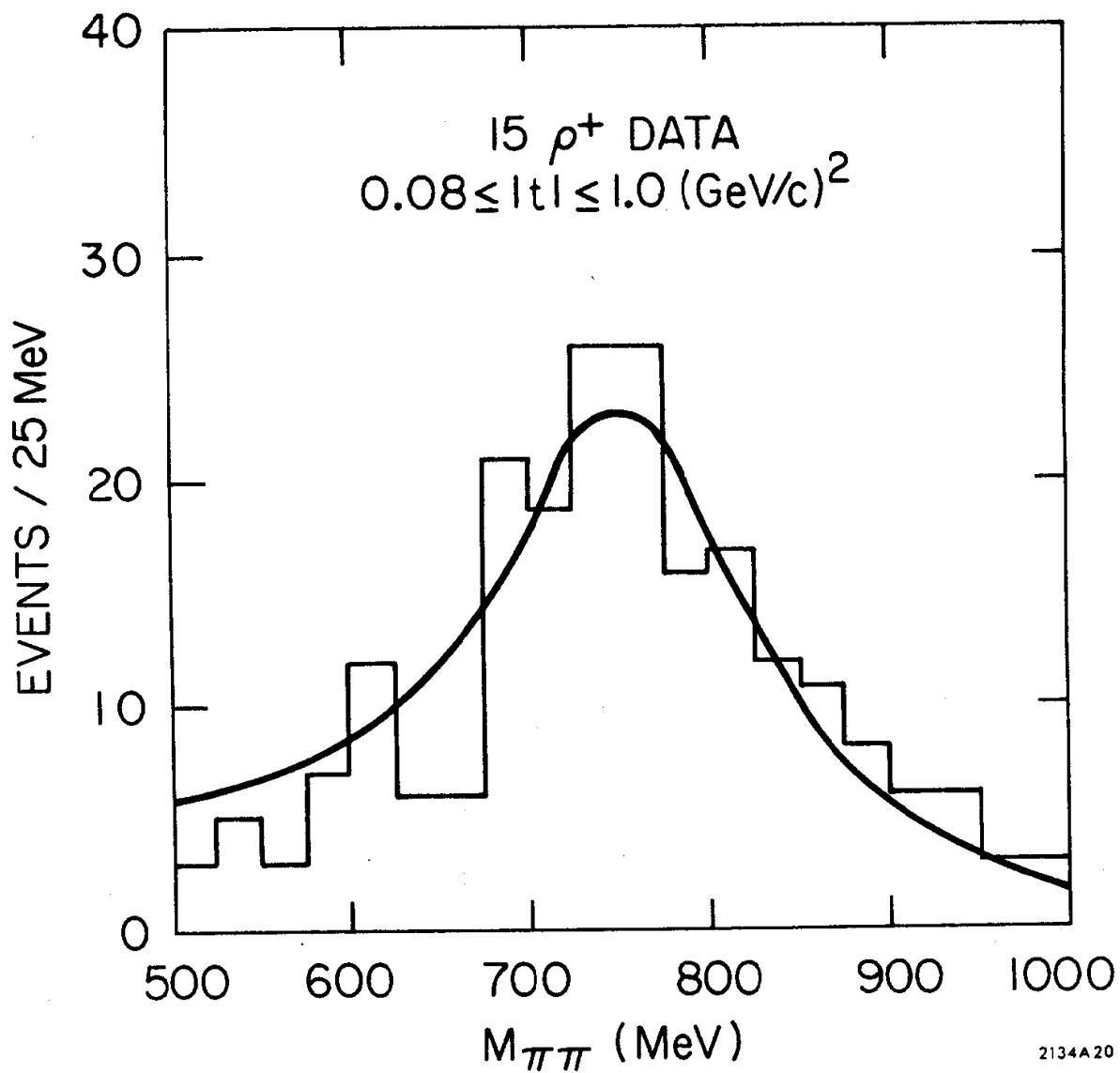
FIG. 17--Typical $M_{\pi\pi}$ spectrum and associated theoretical fit (see text).

TABLE 3

BACKGROUNDS AND CONTAMINATIONS FROM $\pi\pi$ MASS FITS

$\dfrac{-t}{\text{(GeV/c)}^2}$	$15\rho^+$	$15\rho^-$	$15\rho^0$
.000 - .015	12 ± 6%	12 ± 5%	8 ± 5%
.015 - .030	6 ± 4%	7 ± 5%	6 ± 5%
.030 - .045	9 ± 5%	8 ± 6%	18 ± 6%
.045 - .06	16 ± 8%	15 ± 8%	15 ± 7%
.06 - .08	18 ± 10%	26 ± 13%	16 ± 8%
.08 - 1.0	10 ± 9%	16 ± 8%	15 ± 7%

Thus, we need to study the $\pi\pi$ mass structure of the $\rho^\pm$ contamination events; fortunately our experimental design enables us to do this.

As previously mentioned, we are able to isolate high-t $\rho^\pm$ contaminations. These are events which our analysis programs determine to be in the high-t region but which have no observed proton, as they should if they are from the channel $\pi^+\pi^0 p$. Either they are contaminations or the proton has been lost through some inefficiency. We have argued in Chapter II, Section J, that the spark chamber efficiency is high but in Chapter III, Section J, found a 16 ± 5% inefficiency in the data analysis process to find a proton. An appropriate subtraction must be, and has been, made from our high-t contamination samples.

Figure 18 contains the results. Only a small ρ signal is seen in the $M_{\pi\pi}$ distribution. As we are going to eventually argue that the ρ component of the contamination is small, we point out now that the remaining ρ signals can be fully explained by a 5-10% inefficiency in the TV counters.

We also show in Fig. 18 the t-distribution of the contamination events.
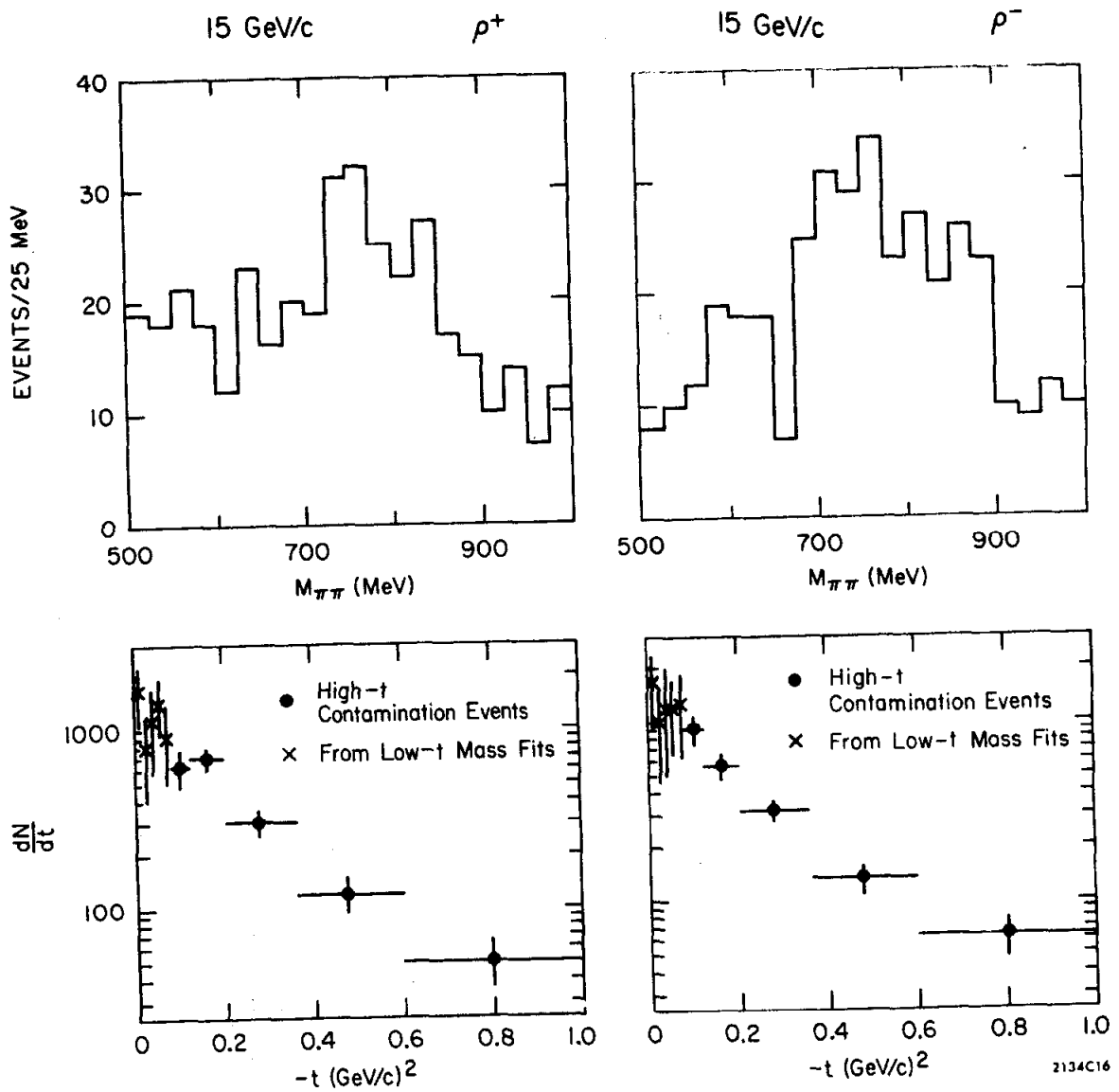
FIG. 18--Mass and momentum transfer distributions of the high-t sample
of contamination events. The low-t backgrounds obtained from
the mass fits are also shown.

The dependence is, within statistics, exponential. We have also plotted, in the low-t region $\left[|t| \leq .08 \text{ (GeV/c)}^2\right]$, the results from the $\pi\pi$ mass fits. Notice that the points from these two classes of events seem to fall on the same curve, suggesting that the two classes may be, in fact, identical. This would mean that the low-t events samples by the $\pi\pi$ mass fits contain no appreciable backgrounds and that the contamination samples exhibit no appreciable ρ structure in $M_{\pi\pi}$.

We have already argued that our data is consistent with the second implication, that the contaminations exhibit no ρ structure. But is it also consistent with the implication that the low-t backgrounds are small? We can gain more information about this by studying the $\pi\pi$ angular distribution. As discussed in this chapter, Section B, the presence of a s-wave background may maifest itself in non-zero values of the density matrix elements $\text{Re } \rho_{S0}^H$ and Re_{S1}^H which measure the interference between the s and p-waves. Fig. 19 shows these elements.

A clear s-wave background is found in the ρ^0 data. The $\rho^\pm$ data is, on the other hand, consistent with no low-t background at all. Actually, it would be somewhat surprising if we did find a very large s-wave term in the $\rho^\pm$ data. A simple symmetry argument, based on the Bose statistics of the $\pi\pi$ state, shows that I + J is even where I and J are the isospin and relative angular momentum of the $\pi\pi$ state. In the ρ^0 case the s-wave state can have either I=0 or I=2 while in the $\rho^\pm$ cases I=0 is prohibited. Since low quantum numbers are favored we would expect this $\rho^\pm$ s-wave to be suppressed relative to the ρ^0 which is, after all, only $\sim 12\%$.

We put all these results together and conclude that the $\pi^\pm\pi^0$ low-t data has a contamination but no s-wave background, that the contamination has no appreciable ρ structure, and that the amount of the contamination can be
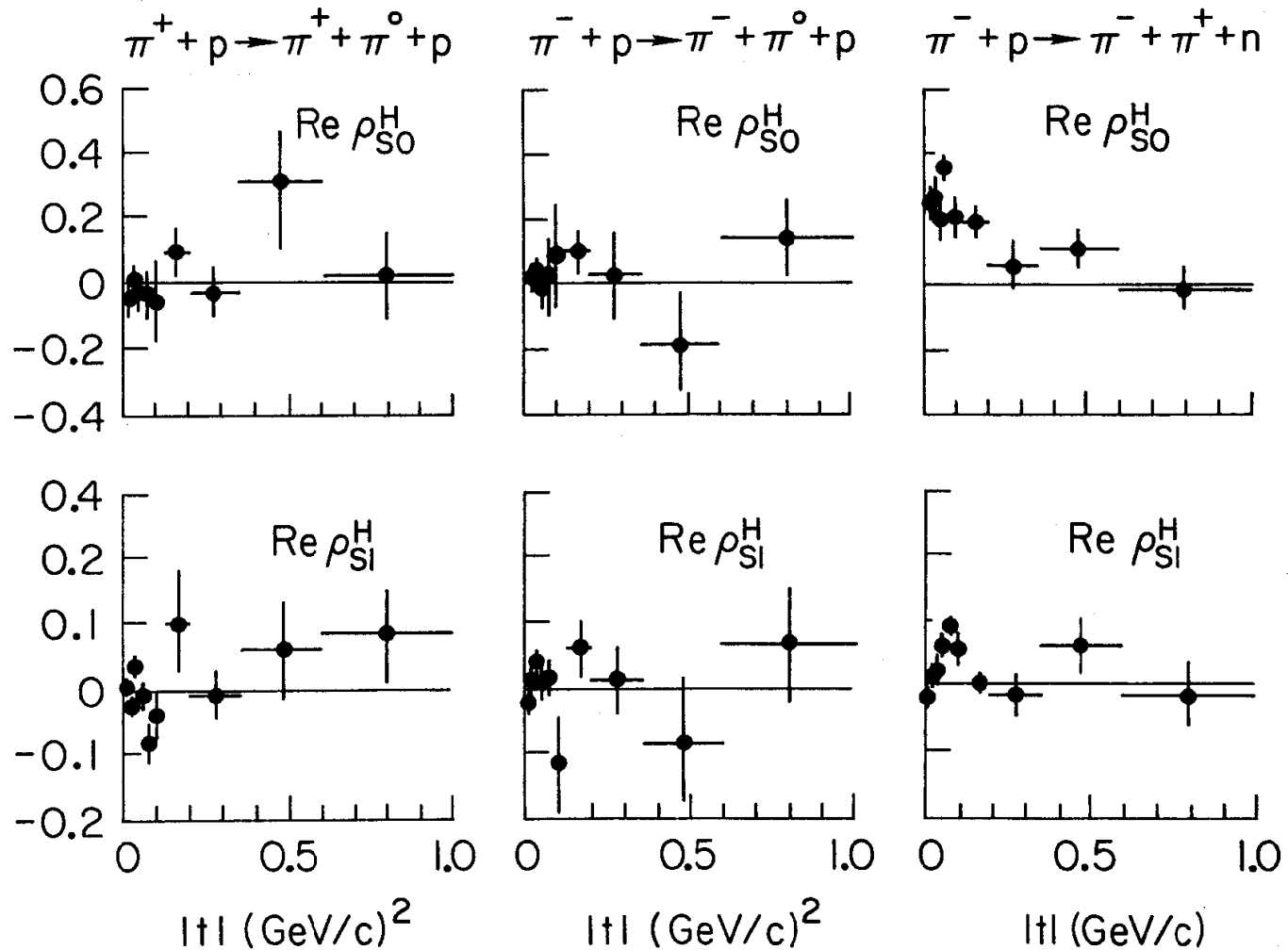
FIG. 19—The s-p wave interference density matrix elements as a function of momentum transfer for the reactions $\pi^{\pm}p \to \rho^{\pm}p$ and $\pi^{-}p \to \rho^{0}n$.

adequately determined from the $\pi\pi$ mass fits. In the high-t $\rho^{\pm}$ data a small

background subtraction, determined from the $\pi\pi$ mass fits, must be made.

A s-wave background subtraction, determined from $\pi\pi$ mass fitting,

must also be made to the ρ^{o} data. In addition, in Section G of Chapter II

we identified a $5 \pm 5\%$ $\rho^{o}\Delta^{o}$ contamination which must be subtracted.

Corrections to the density matrices for these contaminations must also

be made. In all cases, except for the $\rho^{o}\Delta^{o}$ contaminations, we have assumed

the average $\pi\pi$ angular distrbution to be isotropic. For the $\rho^{o}\Delta^{o}$ contamination

we assumed the same angular distribution as the $\rho^{o}n$ signal; this approximation

is not good for very small t ($|t| < m_{\pi}^{2}$) but is adequate for our purposes.

Some caution is in order for we can not rule out the possibility of a

ρ-like contamination with a considerably steeper slope than that shown in

Fig. 18. This contamination would be small in the high-t region but could

be of quite significant size for low values of t. In fact, the typical particle

production cross sections tend to have slopes of 8-11 $(GeV/c)^{-2}$ whereas the

slopes of the overall contamination, shown in Fig. 18, are around 5 $(GeV/c)^{-2}$.

The possible systematic error has been estimated by taking a slope of

12 $(GeV/c)^{-2}$; we use the conservative figure of $\pm 15\%$.

E. $\underline{d\sigma/dt \text{ and } \rho^{H}_{mm}}$,

To compute the cross section we must normalize the experiment. The

beam and electronics used in monitoring the beam were discussed in Chapter

II. Table 4 lists the total beam fluxes after correction for the K, μ, and p

contaminations; the errors shown are purely statistical in origin.

The hydrogen target was (50.0 ± 0.5) cm long and was operated at an

average pressure of 33.5 ± 3 psi corresponding to a number density of

$(.405 \pm .005) \times 10^{23} cm^{-3}$.

TABLE 4

TOTAL π FLUXES THROUGH THE HYDROGEN TARGET

Data Point	Total π
15 ρ^+ (target full)	$(72.6 \pm 0.4) \times 10^6$
15 ρ^- (target full)	$(71.7 \pm 0.4) \times 10^6$
15 ρ^0 (target full)	$(40.2 \pm 0.3) \times 10^6$

The target empty corrections in this experiment have turned out to be small. Within statistics the target empty t-distributions and $\pi\pi$ angular distribution are the same as the target full and so represent only a normalization correction. Table 5 gives the actual values; the errors shown are statistical. The systematic uncertainty is small.

TABLE 5

TARGET EMPTY SUBTRACTIONS

Data Point	Target Empty Subtractions
15ρ^+	$6.7 \pm 2.3\%$
15ρ^-	$9.4 \pm 2.6\%$
15ρ^0	$0.6 \pm 0.4\%$

In our analysis we have only included events such that $665 \leq M_{\pi\pi} \leq 865$ MeV. As a model to estimate the number of ρ events excluded by this cut, we have used a relativistic Breit-Wigner[18]: 43% are lost. This correction depends on which Breit-Wigner form one chooses; we estimate the resulting systematic uncertainty in the overall normalization to be $\pm 15\%$.

After all the corrections detailed in this chapter, we arrive at the ρ cross sections and density matrix elements (in the helicity frame) which are shown in Fig. 20 and Fig. 21; the errors included only statistical effects. The s-wave
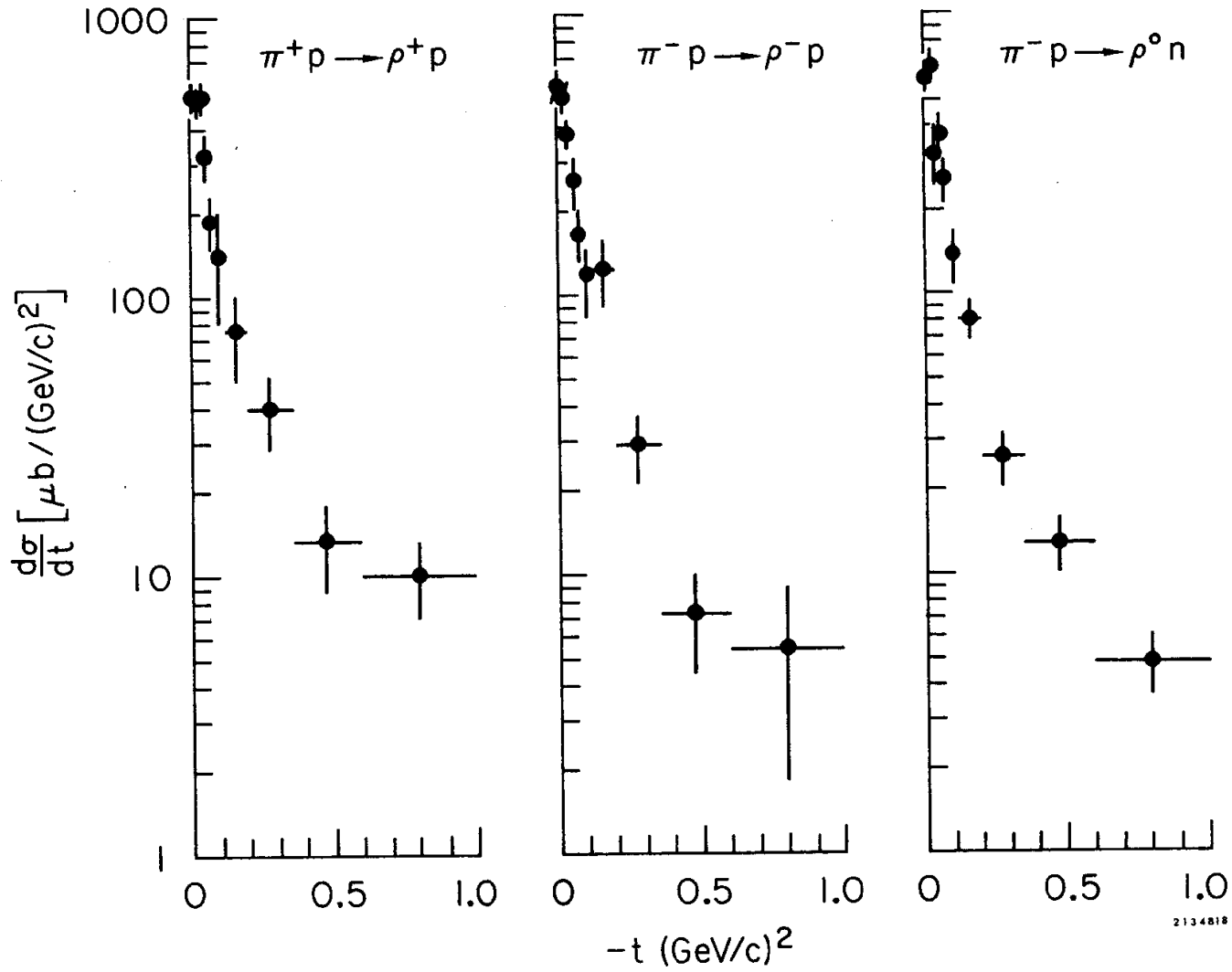
FIG. 20--The differential cross sections as a function of momentum transfer for the reactions $\pi^{\pm}p \to \rho^{\pm}p$ and $\pi^-p \to \rho^0 n$.
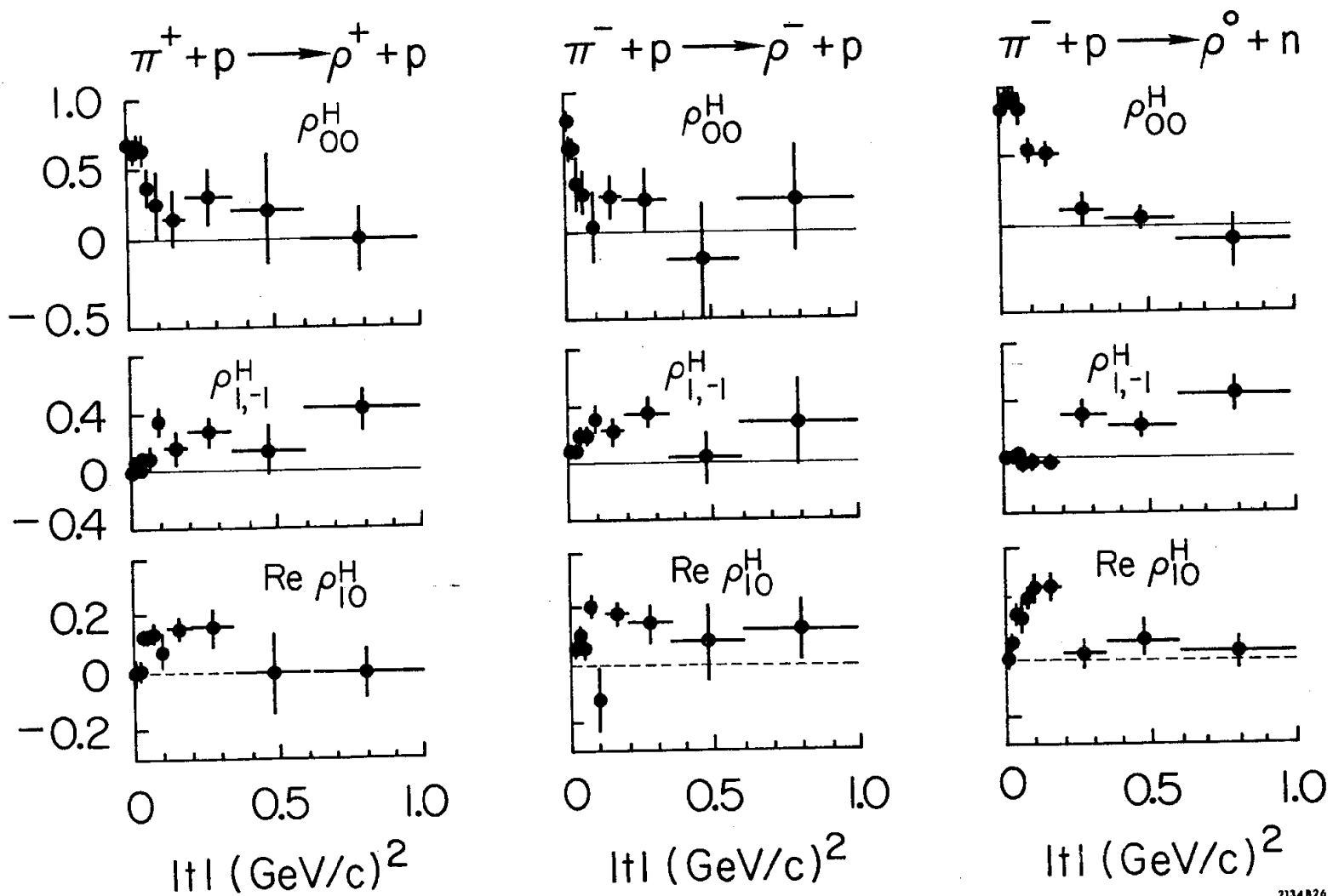
FIG. 21--The ρ density matrix elements as a function of momentum transfer for the reactions $\pi^{\pm}p \to \rho^{\pm}p$ and $\pi^{-}p \to \rho^{0}n$.

subtractions have been made so that the density matrix normalization is

$$\rho_{00}^{H} + 2\rho_{11}^{H} = 1$$

The numerical values for these data are given in Tables 6, 7 and 8.

TABLE 6

$$\frac{d\sigma}{dt}, \ \rho_{mm'}^{H} \quad \text{for } \pi^{+} + p \to \rho^{+} + p \text{ at } 15.0 \text{ GeV/c}$$

$\frac{|t|}{(\text{GeV/c})^2}$	$\frac{d\sigma}{dt} \ \mu b/(\text{GeV/c})^2$	ρ_{00}^{H}	$\rho_{1,-1}^{H}$	$\text{Re } \rho_{10}^{H}$
.000 − .015	533 ± 65	.70 ± .09	.00 ± .04	.00 ± .04
.015 − .030	504 ± 65	.63 ± .08	.07 ± .03	.01 ± .04
.030 − .045	526 ± 65	.67 ± .07	.02 ± .03	.13 ± .03
.045 − .060	320 ± 60	.65 ± 12	.11 ± .03	.13 ± .03
.06 − .08	190 ± 40	.38 ± .15	.11 ± .07	.14 ± .06
.08 − .12	139 ± 35	.25 ± 25	.36 ± 10	.08 ± .06
.12 − .20	75 ± 25	.15 ± .21	.17 ± .12	.16 ± .07
.20 − .35	40 ± 12	.33 ± .19	.28 ± .11	.16 ± .06
.35 − .60	13 ± 5	.23 ± .40	.15 ± .17	.00 ± .14
.60 − 1.0	10 ± 3	.00 ± .25	.43 ± .14	.00 ± .09

Only statistical errors are shown

Density matrix in helicity frame

TABLE 7

$$\frac{d\sigma}{dt}, \; \rho^H_{mm'} \; \text{ for } \pi^- + p \rightarrow \rho^- + p \text{ at } 15.0 \text{ GeV/c}$$

$\frac{|t|}{(GeV/c)^2}$	$\frac{d\sigma}{dt} \; \mu b/(GeV/c)^2$	ρ^H_{00}	$\rho^H_{1,-1}$	Re ρ^H_{10}
.000 – .015	559 ± 70	.78 ± .08	.03 ± .02	.08 ± .03
.015 – .030	515 ± 70	.61 ± .09	.07 ± .03	.08 ± .03
.030 – .045	383 ± 55	.60 ± .09	.07 ± .04	.11 ± .03
.045 – .060	256 ± 55	.34 ± .20	.21 ± .06	.06 ± .04
.06 – .08	165 ± 35	.30 ± .16	.19 ± .06	.21 ± .03
.08 – .12	118 ± 27	.05 ± .25	.32 ± .10	-.12 ± .09
.12 – .20	123 ± 32	.26 ± .16	.22 ± .09	.18 ± .04
.20 – .35	29 ± 8	.23 ± .23	.35 ± .12	.14 ± .07
.35 – .60	7 ± 3	-.19 ± .40	.03 ± .18	.08 ± .14
.60 –1.00	5 ± 4	.25 ± .36	.28 ± .30	.12 ± .11

Only statistical errors are shown

Density Matrix in helicity frame

TABLE 8

$$\frac{d\sigma}{dt}, \rho^H_{mm'} \text{ for } \pi^- + p \rightarrow \rho^o + n \text{ at } 15.0 \text{ GeV/c}$$

$\frac{|t|}{(\text{GeV/c})^2}$	$\frac{d\sigma}{dt} \mu b/(\text{GeV/c})^2$	ρ^H_{00}	$\rho^H_{1,-1}$	$\text{Re } \rho^H_{10}$
.000 - .015	595 ± 72	.82 ± .08	.01 ± .03	.00 ± .03
.015 - .030	658 ± 83	.89 ± .07	-.01 ± .03	.05 ± .03
.030 - .045	286 ± 60	.88 ± .08	-.02 ± .03	.16 ± .05
.045 - .060	340 ± 65	.91 ± .10	.02 ± .02	.14 ± .06
.060 - .080	235 ± 42	.83 ± .11	-.07 ± .04	.21 ± .03
.08 - .12	125 ± 25	.53 ± .10	-.02 ± .04	.24 ± .05
.12 - .20	75 ± 14	.51 ± .07	-.03 ± .04	.25 ± .05
.20 - .35	24 ± 5	.11 ± .13	.36 ± .10	.01 ± .05
.35 - .60	12 ± 3	.06 ± .07	.25 ± .11	.07 ± .07
.60 -1.00	4 ± 1	-.10 ± .20	.52 ± .12	.01 ± .06

Only statistical errors are shown

Density matrix in helicity frame

F. Overall Statistical and Systematic Errors

We plan, ultimately, to use Eq. (1.3) to derive the cross sections and density matrix elements for the reaction $\pi^O + p \to \rho^O + p$. As many of the corrections apply to all three states of the ρ, the systematic and some overall statistical uncertainties will tend to cancel. It is important to estimate the correlations in this experiment.

First consider the statistical uncertainties, for example, the target empty subtractions. The statistical errors in these subtractions are large because of our limited sample, but uncorrelated since the subtractions are determined independently for each data point.

Another example is the data analysis inefficiency correction discussed at the end of Chapter III. Here we assumed the ρ^+ and ρ^- corrections were equal and used the average for both points; the ρ^+ and ρ^- corrections are completely correlated in this case. Table 9 tabulates the overall statistical corrections and the ρ^+/ρ^- correlations. At the bottom we have listed the total overall statistical corrections and correlations.

Table 10 gives the equivalent list of significant overall systematic errors. We have estimated some of the $\rho^\pm/\rho^O$ correlations as 0.5; this is because there is some similarity but not complete equivalence in the $\rho^\pm$ and ρ^O corrections. For example, we estimate the systematic uncertainty in the acceptance corrections as $\pm 5\%$; the $\rho^\pm$ and ρ^O corrections are similar in that they both include the acceptance of a $\pi^\pm$ but different in that the $\rho^\pm$ involves the acceptance of two photons instead of a π^+ as does the ρ^O.

At the end of Table 10 we have totalled up the corrections and correlations assuming each type of correction to be independently estimated (i.e., the errors from different corrections have been added in quadrature).

TABLE 9

OVERALL STATISTICAL ERRORS

Source	ρ^+	ρ^-	ρ^o	Correlation ρ^+/ρ^o	Correlation $\rho^\pm/\rho^o$
Data Analysis Efficiency	4%	4%	5%	1.0	0.0
Picture Veto Losses	3%	3%	0%	1.0	0.0
Normalization	1.7%	1.7%	1.8%	0.0	0.0
Target Empty Subtraction	2.5%	2.5%	0.4%	0.0	0.0
Total	6%	6%	5%	0.7	0.0

In Table 10 we have not included the systematic uncertainty in the subtraction of the $\rho^\pm$ contamination, discussed in Section D of this chapter, since it is not an overall uncertainty but applies only to the low-t $\rho^\pm$ region. We estimated this uncertainty to be ±15%, and will keep track of it separately.

TABLE 10

OVERALL SYSTEMATIC ERRORS

Source	$\rho^\pm$	ρ^-	ρ^o	Correlation ρ^+/ρ^-	Correlation $\rho^\pm/\rho^o$
Absorption Losses	2%	±2%	±1%	1.0	0.5
Neutron Vetoes	--	--	±3%	--	--
Apparatus Inefficiency	5%	5%	2%	1.0	0.5
Data Analysis Inefficiency	5%	5%	5%	1.0	0.5
Acceptance Correction	5%	5%	5%	1.0	0.5
S-wave Subtraction	5%	5%	5%	1.0	0.5
Normalization	2%	2%	2%	1.0	1.0
Mass Cut Correction	±15%	±15%	±15%	1.0	1.0
Δ^o Subtraction For ρ^o	--	--	5%	--	--
Total	19%	19%	18%	1.0	0.8

CHAPTER V

DISCUSSION OF THE REACTIONS $\pi^{\pm} + p \to \rho^{\pm} + p$

At the end of Chapter IV we gave the differential cross sections and density matrix elements for the reactions $\pi^{\pm} + p \to \rho^{\pm} + p$. The basic aim of this paper is to combine these measurements to study the reaction $\pi^0 + p \to \rho^0 + p$. However, in this chapter we briefly discuss these channels as separate entities.

Looking at Fig. 20 we see that, as expected from other measurements, the differential cross section is dominated by a sharp forward peak. Most of the total channel cross section comes from the range $0 \le |t| \le 0.5 \, (\text{GeV/c})^2$. Thus, the total channel cross section $\sigma(\pi^{\pm} p \to \rho^{\pm} p)$ is to good approximation only a measure of the forward peak. We find

$$\sigma(\pi^+ p \to \rho^+ p) = 50 \pm 9 \, \mu b$$

$$\sigma(\pi^- p \to \rho^- p) = 47 \pm 9 \, \mu b$$

The errors include the $\pm 17\%$ overall systematic uncertainty previously discussed.

In Fig. 22 we plot these total cross section values as a function of p_{LAB}, the total incident laboratory momentum. We also include lower energy bubble chamber data[20] on this plot. We have fit to this data the conventional equation

$$\sigma = K \, p_{LAB}^{-n}.$$

We find

$$n(\pi^+ p \to \rho^+ p) = 1.80 \pm 0.08$$

$$n(\pi^- p \to \rho^- p) = 1.87 \pm 0.15.$$
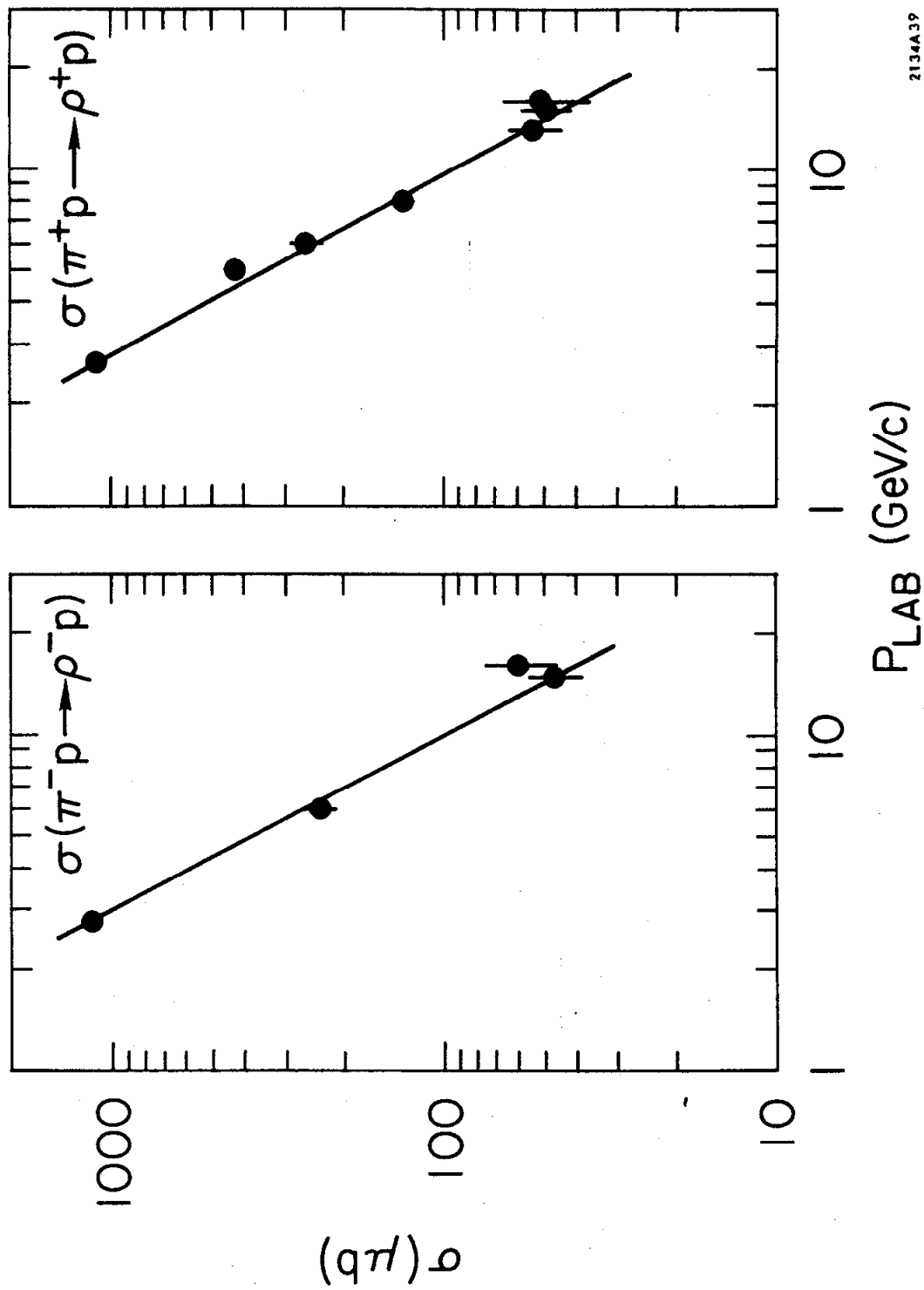
FIG. 22--The energy dependence of the cross sections for $\pi^{\pm}p \to \rho^{\pm}p$. Reference 20 traces the sources used in this figure.

2134A39

These results are in good agreement with other determinations of this quantity.[21]

Returning to the shape of the forward peaks in Fig. 20, we find that for $|t| \gtrsim 0.03$ $(GeV/c)^2$ our $d\sigma/dt$'s are in fair agreement with a bubble chamber measurement [10] at 16 GeV/c. And our $d\sigma/dt$'s represent reasonable extrapolations of lower energy $d\sigma/dt$ measurements. But for $|t| \lesssim 0.03$ $(GeV/c)^2$ we must observe that we have not been able to resolve one of the questions which led us to carry out this experiment. With large errors $d\sigma/dt$ $(\pi^- p \rightarrow \rho^- p)$ shows a peak as $t \rightarrow 0$, while $d\sigma/dt(\pi^+ p \rightarrow \rho^+ p)$ is roughly flat as $t \rightarrow 0$. This is in disagreement with the hydrogen bubble chamber results[10] at 16 GeV/c. The bubble chamber data shows a dip in both differential cross sections as $t \rightarrow 0$.

Now, the basic experimental question is whether the bubble chamber experiments have a bias against finding low-t events in the reactions $\pi^\pm + p \rightarrow \rho^\pm + p$. This bias could occur in scanning because the low-t events have short proton tracks and may have a small angle between the initial and final charged pion tracks. There is disagreement between experimentalists as to whether this bias can be tested for and corrected. The experimenters who carried out the 16 GeV/c bubble chamber measurement looked for this bias, found it only in one of the reactions, and corrected for it. On the other hand, the authors of a paper describing a 6 GeV/c bubble chamber measurement of these reactions[8] believed that there is a significant scanning loss for $|t| < 0.1$ $(GeV/c)^2$ events, even at this lower energy where the bias should be less severe. Therefore, they do not use their data for $|t| < 0.1$ $(GeV/c)^2$.

In our experiment we had hoped to resolve this question for we do not have a bias against low-t events. We do not see the forward dip observed

in the bubble chamber experiment, but we have the possibility of the lowest-t bins having an excess of events through contamination by events from other topologies. We have discussed this in detail in the previous chapters; we do not believe that there could be sufficient contamination to fill in the dip, but we cannot prove this. Therefore, we regard the question as to the very small-t behavior of the reactions $\pi^{\pm} + p \rightarrow \rho^{\pm} + p$ as still unresolved.

The theoretical prejudice is certainly that a very forward dip should exist, but it is wrong for an experimentalist to be swayed in his observation by this consideration.

THE REACTION $\pi^0 + p \rightarrow \rho^0 + p$ AND CONCLUSIONS

A. Calculation of $\frac{d\sigma}{dt}$ and $\rho_{mm'}^H$, for $\pi^0 + p \rightarrow \rho^0 + p$

In Chapter I we deduced the following formulae:

$$\frac{d\sigma}{dt}(\pi^0 p \rightarrow \rho^0 p) = \frac{1}{2}\left[-\frac{d\sigma}{dt}(\pi^+ p \rightarrow \rho^+ p) + \frac{d\sigma}{dt}(\pi^- p \rightarrow \rho^- p) - \frac{d\sigma}{dt}(\pi^- p \rightarrow \rho^0 n)\right]$$

(6.1)

$$\rho_{\mu\nu}^H \frac{d\sigma}{dt}(\pi^0 p \rightarrow \rho^0 p) = \frac{1}{2}\left[\rho_{\mu\nu}^H \frac{d\sigma}{dt}(\pi^+ p \rightarrow \rho^+ p) + \rho_{\mu\nu}^H \frac{d\sigma}{dt}(\pi^- p \rightarrow \rho^- p)\right.$$

$$\left. - \rho_{\mu\nu}^H \frac{d\sigma}{dt}(\pi^- p \rightarrow \rho^0 n)\right]$$

(6.2)

Because of various correlations some care in the propagation of errors through these formulae must be exercised. We have already touched on the subject of correlations in the systematic errors (Section F, Chapter IV). Because of the loss of acceptance when $\cos \Theta_\rho^* \rightarrow \pm 1$ there are also correlations in the statistical errors on $\rho_{mm'}^H$ and $\frac{d\sigma}{dt}$. In particular, ρ_{00}^H and $\frac{d\sigma}{dt}$ are strongly correlated. These correlations are known and have been systematically used in the error propagation.

By dividing Eq. (6.2) by Eq. (6.1) the density matrix elements for $\pi^0 + p \rightarrow \rho^0 + p$ are obtained. It is advantageous to do this as the systematic errors on $\frac{d\sigma}{dt}$, strongly correlated between the three reactions, tend to cancel. In fact, the systematic errors on $\rho_{mm'}^H (\pi^0 p \rightarrow \rho^0 p)$ turn out to be rather small and will be neglected; on the other hand, the systematic errors on $\frac{d\sigma}{dt} (\pi^0 p \rightarrow \rho^0 p)$ are large and may not be neglected.

The values obtained for $\frac{d\sigma}{dt} (\pi^0 p \rightarrow \rho^0 p)$ are given in Table 11 along with the estimated systematic errors. We have quoted two systematic errors,

TABLE 11

$$\frac{d\sigma}{dt} \text{ And Errors for } \pi^0 + p \rightarrow \rho^0 + p \text{ At } 15.0 \text{ GeV/c}$$

t $(GeV/c)^2$	$\frac{d\sigma}{dt}$ $\left[\mu b/(GeV/c)^2\right]$ *	Overall Systematic $\left[\mu b/(GeV/c)^2\right]$	Low-t Systematic $\left[\mu b/(GeV/c)^2\right]$
.000 – .015	249 ± 60	50	90
.015 – .30	181 ± 65	50	90
.030 – .045	312 ± 55	40	75
.045 – .060	118 ± 55	30	45
.06 – .08	60 ± 35	16	30
.08 – .12	66 ± 25	12	
.12 – .20	61 ± 22	10	
.20 – .35	23 ± 8	3	
.35 – .60	4 ± 3	1	
.60 – 1.00	5 ± 3	1	

*The errors in this column are statistical

an overall systematic error and a low-t systematic associated with the uncertainties in the low-t contamination subtractions. Also, in Table 12 the values for the density matrix elements are listed; only the statistical errors, which are generally at least twice as large as the systematic errors, are listed.

TABLE 12

$\rho^H_{mm'}$, For $\pi^0 + p \rightarrow \rho^0 + p$ At 15.0 GeV/c [*]

$\dfrac{t}{(GeV/c)^2}$	ρ^H_{00}	$\rho^H_{1,-1}$	Re ρ^H_{10}
.000 - .015	.62 ± .60	.02 ± .20	.09 ± .07
.015 - .030	.12 ± .50	.22 ± .20	.01 ± .08
.030 - .045	.53 ± .30	.35 ± .20	.03 ± .12
.045 - .060	-.06 ± .30	.35 ± .20	.03 ± .12
.06 - .08	-.62 ± .40	.57 ± .30	.10 ± .15
.08 - .12	-.18 ± .60	.70 ± .05	-.24 ± .13
.12 - .20	-.20 ± .30	.34 ± .30	.11 ± .11
.20 - .35	.35 ± .30	.30 ± .30	.18 ± .09
.35 - .60	.0 ± .6	.0 ± .6	.0 ± .3
.60 - 1.00	.0 ± .3	.5 ± .5	.0 ± .2

[*]Only statistical errors are shown.

In Fig. 23 we have plotted these data. The systematic uncertainties in the values of $\frac{d\sigma}{dt}$ ($\pi^0 p \rightarrow \rho^0 p$) are indicated, in a general way, by the dotted lines; the data points can move, in a continuous manner, up or down within this error corridor. The statistical errors are indicated by the conventional bars.
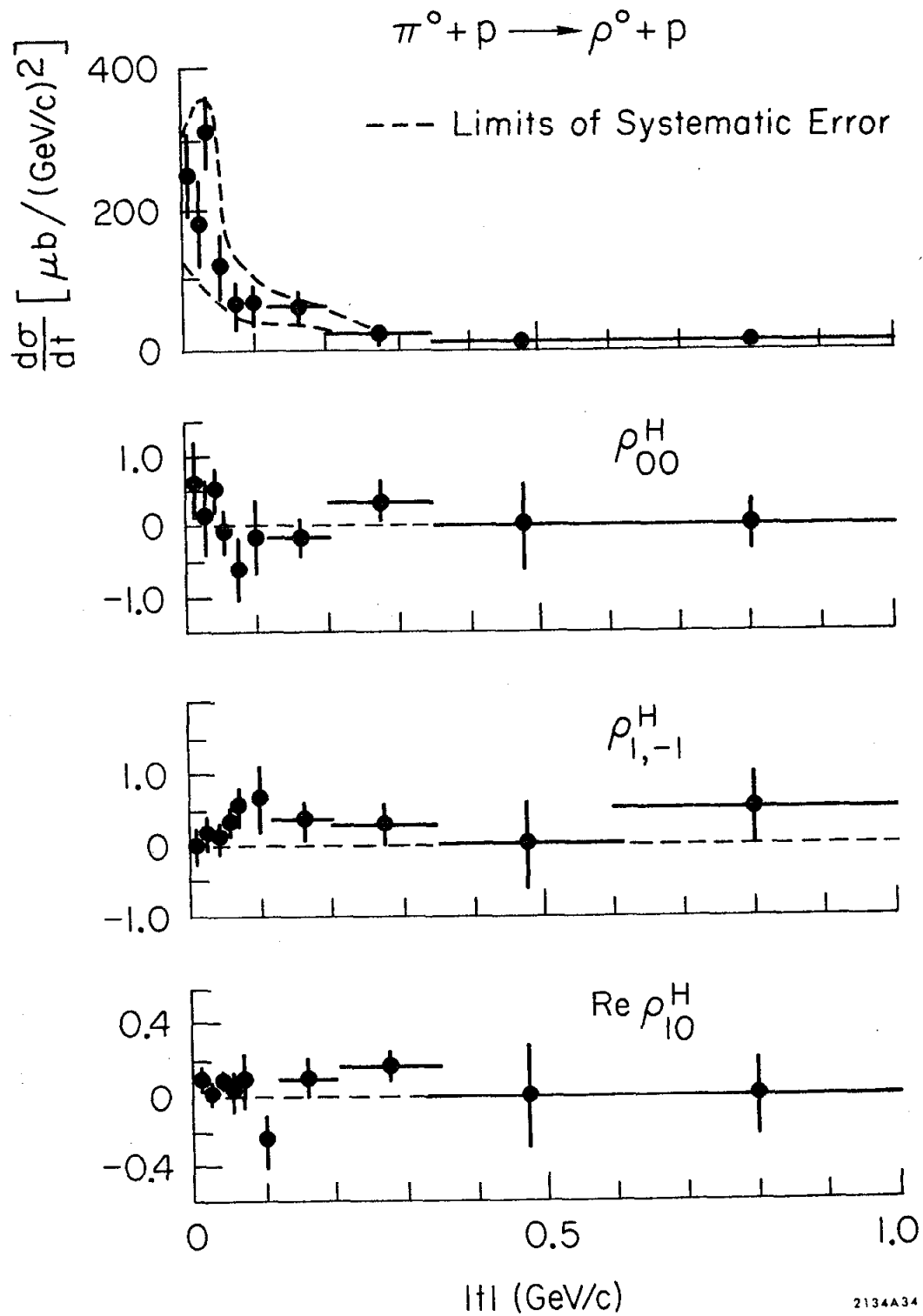
FIG. 23--The cross section and density matrix elements as a function of momentum transfer for the reaction $\pi^0 p \rightarrow \rho^0 p$ at 15.0 GeV/c.

B. Basic Tests of the Data

Cohen-Tannoudji, Salin, and Morel have shown[22] that the exchange of a definite spin-parity in the t-channel leads to general relationships in the s-channel. In particular, parity conservation at the $\pi^0 \rho^0 \omega$ vertex (Fig. 1) implies

$$A_{\mu\lambda_n} = - \eta_e (-1)^{S_e} (-1)^{\mu} A_{-\mu\lambda_n} . \qquad (6.3)$$

$A_{\mu\lambda_n}$ is the amplitude for $\pi^0 + p \rightarrow \rho^0 + p$ where the ρ^0 has a helicity μ, the incident and final protons have helicity λ_n, and the particle exchanged in the t-channel has spin S_e and parity η_e. As we discussed in Chapter I, the reaction $\pi^0 + p \rightarrow \rho^0 + p$ is expected to be dominated by ω-exchange in the t-channel. As the ω is a vector particle, Eq. (6.3) immediately yields $A_{0\lambda_n} = 0$ leading to the prediction

$$\rho^H_{00} = 0. \qquad (6.4)$$

Before testing our data against this prediction, however, we must determine the possible effect of the so-called absorptive corrections on Eq. (6.4). These corrections refer to the loss of the initial and final state particles (Fig. 1) because of secondary interactions. Gottfried and Jackson, in their pioneering paper[17] on this subject, show that the calculation of absorption corrections is formally equivalent to the calculation of the two diagrams shown in Fig. 24. In these diagrams the bubbles represent elastic scattering. The connection to elastic scattering occurs through the optical model assumption that the elastic scattering is purely a shadow of the inelastic processes. Thus, the experimental fact that helicity is conserved in elastic scattering,[23] when applied to the diagrams of Fig. 24, leads to the conclusion that Eq. (6.4) continues to hold when initial and

- 78 -
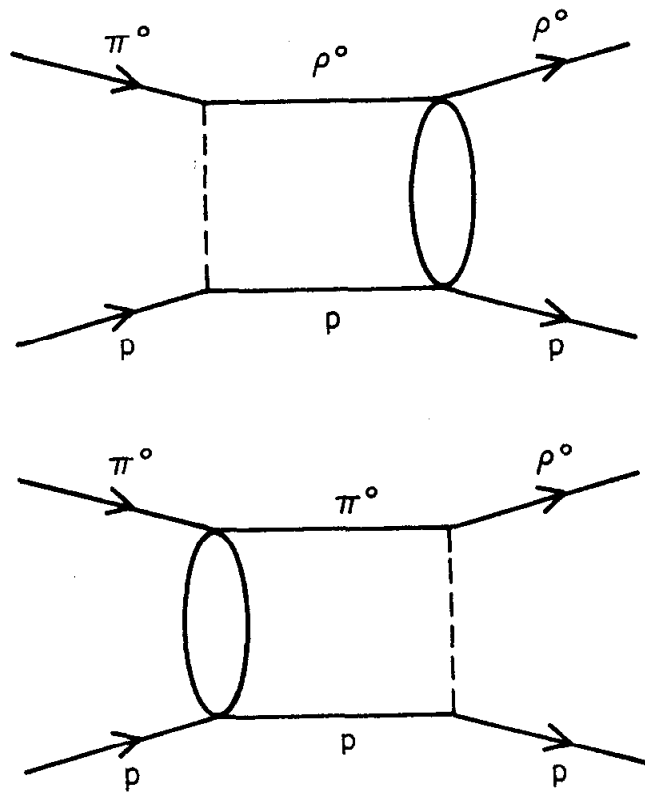
2134A35

FIG. 24--Absorption corrections to the reaction $\pi^0 p \to \rho^0 p$. The bubbles represent elastic scattering.

final state absorption is taken into account.

Our data, shown in Fig. 23, is consistent with (6.2) and thus consistent with simple ω-exchange. It would, in fact, be rather amazing if we found (6.2) not true because of the generality of the arguments leading to it; yet, two out of the three other experiments (discussed in Section C of Chapter I) find large values of ρ_{00}^{H} . These two are the experiment at 2.67 GeV/c[6] and the experiment at 16.0 GeV/c[10]; the experiment at 6.0 GeV/c[8] and our experiment at 15.0 GeV/c find values of ρ_{00}^{H} consistent with zero.

The situation is very confusing; the conclusion made in this paper is that these nonzero values of ρ_{00}^{H} are most likely the result of systematic problems. When we use data from these other experiments, the errors on their cross sections will be accordingly increased.

C. Comparison with Other Experiments; The Dual-Absorption Model

The 16.0 GeV/c data[10] for $\pi^{o} + p \rightarrow \rho^{o} + p$ has been fit with the form predicted by the dual-absorption model[9]; this expression has already been given as Eq. (1.6). An excellent fit to this data was obtained with $\chi^{3} = 3$ for 11 degrees of freedom. We have extrapolated this 16.0 GeV/c fit to our energy using a similar 6.0 GeV/c fit[8] as a guide. Fig. 25 shows the result which is basically a comparison of our data to the 16.0 GeV/c data.

The agreement is not impressive. While our data is consistent with the dip at $|t| \sim 0.5$ $(GeV/c)^{2}$, the disagreement in the region $0 \lesssim |t| \lesssim 0.3$ $(GeV/c)^{2}$ exceeds any known systematic effects. Furthermore, our data shows no signs of the dip expected in the dual-absorption model as $|t| \rightarrow 0.0$ $(GeV/c)^{2}$. As discussed in Chapter V, this lack of a dip in
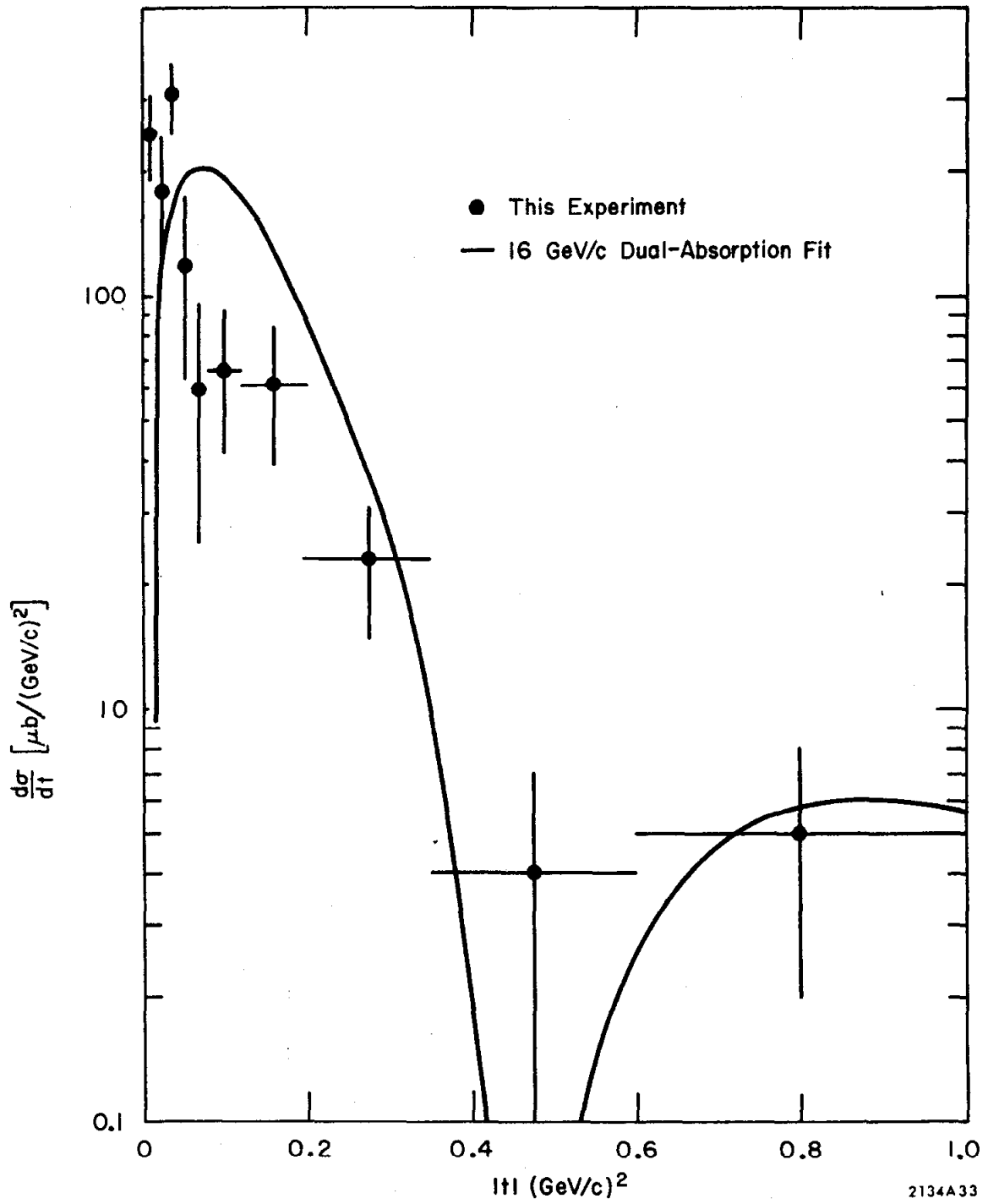
FIG. 25—Comparison of our measurement of the cross section for $\pi^0 p \rightarrow \rho^0 p$ with the dual-absorption fit to the 16.0 GeV/c data.

$\frac{d\sigma}{dt}(\pi^0 p \to \rho^0 p)$ results from the lack of any dip structure as $t \to 0.0$ $(\text{GeV/c})^2$ in our measurements of $\frac{d\sigma}{dt}(\pi^\pm p \to \rho^\pm p)$. There, we concluded that our measurements in the small-t region could have a background contamination, and the same reservation must be held about our data on $\pi^0 + p \to \rho^0 + p$ as $|t| \to 0.0 (\text{GeV/c})^2$.

D. <u>Energy Dependence of $\sigma_p(\pi^0 p \to \rho^0 p)$</u>

In this section the energy dependence of $\sigma_p(\pi^0 p \to \rho^0 p)$, defined as

$$\sigma_p(\pi^0 p \to \rho^0 p) = \int_0^{1.0(\text{GeV/c})^2} \frac{d\sigma}{dt}(\pi^0 p \to \rho^0 p) \, dt, \tag{6.5}$$

will be studied from two points of view. To obtain the energy dependence we have used data from three other experiments.[6, 8, 10] As disucssed in Section B of this chapter, two of these experiments[6, 10] have what may be anomalous values of $\rho_{00}^H(\pi^0 p \to \rho^0 p)$. Since we think these values arise from systematic effects which can become very severe when one performs the subtractions of Eqs. (6.1) and (6.2) we have correspondingly enlarged the errors on (6.5) for these experiments.

A fit of the conventional form

$$\sigma \propto P_{LAB}^{-n} \tag{6.6}$$

to these data gives $n = 1.44 \pm 0.25$.

To study the energy dependence in more detail we have used some simple ideas from Regge theory.[24] The simple Regge form for the differential cross section is

$$\frac{d\sigma}{dt} = Ce^{2\alpha(t)-2} \tag{6.7}$$

$\alpha(t)$ is the trajectory function for the ω-meson. With the convenient para-

meterization $\alpha(t) = \alpha_0 - \alpha_1 t$, we obtain

$$\sigma_p(\pi^0 p \to \rho^0 p) \approx C \frac{s^{2\alpha_0 - 2}}{\ell n s} . \tag{6.8}$$

Fig. 26 shows the result of a fit of this form to the data. We find:

$$\alpha_0 = 0.42 \pm 0.13. \tag{6.9}$$

An experiment studying the reaction $K_L^0 + p \to K_S^0 + p$ has determined the ω-trajectory intercept[25] to be

$$\alpha_0 = 0.47 \pm 0.09,$$

in good agreement with the value obtained in this experiment.

E. Comparison of $\pi^0 + p \to \rho^0 + p$ and $\gamma + p \to \pi^0 + p$; the Vector Dominance Model

The Vector Dominance model (VDM) attempts to explain the hadronic interactions of the photon by assuming the photon to be coupled to the known vector mesons.[26] The VDM prediction for $\gamma + p \to \pi^0 + p$ is shown in Fig. 27 and reads

$$A_\lambda(\gamma p \to \pi^0 p) = \frac{e}{2\gamma_\rho} A_\lambda(\pi^0 p \to \rho^0 p) + \frac{e}{2\gamma_\omega} A_\lambda(\pi^0 p \to \omega p) \tag{6.10}$$

We have neglected the third term in Fig. 27 because of the experimentally observed weak coupling of the Φ to non-strange mesons.[4,5] The photon, and vector meson helicity, is λ; the nucleon helicities are not explicitly shown. The relative phase space factors are approximately one at high energies. Then,

$$\frac{d\sigma}{dt}(\gamma p \to \pi^0 p) = \frac{1}{2} \sum_{\lambda = \pm 1} \left| A_\lambda(\gamma p \to \pi^0 p) \right|^2 ,$$
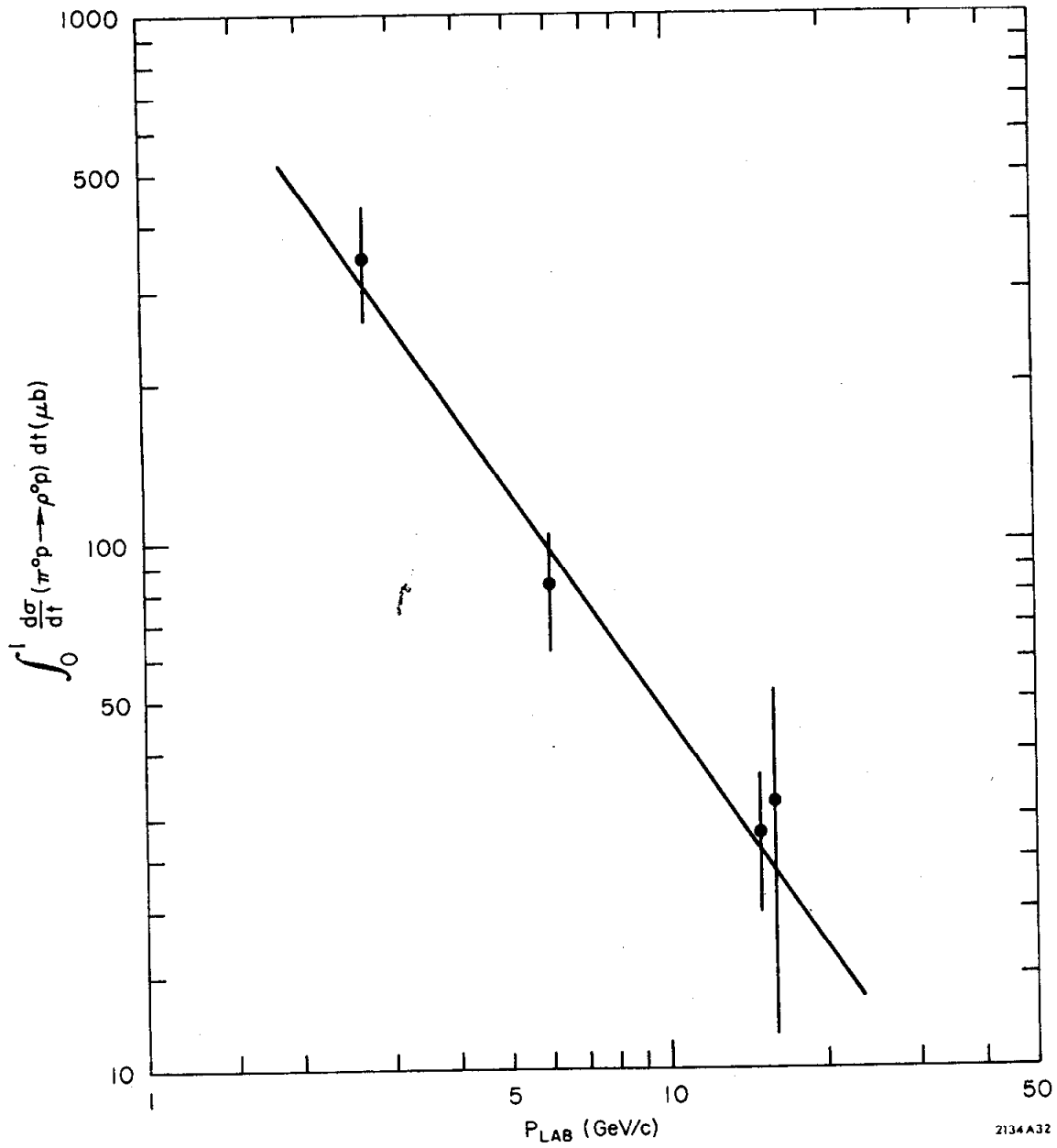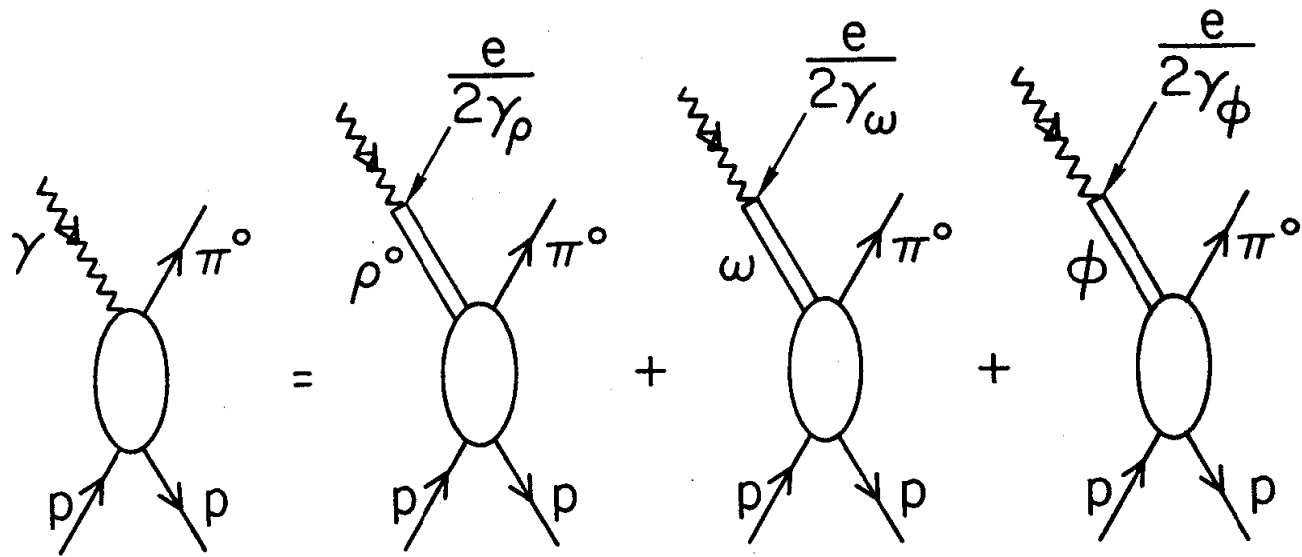
FIG. 26--The energy dependence of the cross section for $\pi^0 p \to \rho^0 p$. The curve is a fit of a Regge form (see text).

FIG. 27—Vector dominance expansion for the reaction $\gamma p \rightarrow \pi^0 p$.

2134A36

or

$$\frac{8}{\alpha}\left(\frac{\gamma_\rho^2}{4\pi}\right)\frac{d\sigma}{dt}(\gamma p \to \pi^o p) = 2\rho_{11}^H \frac{d\sigma}{dt}(\pi^o p \to \rho^o p) + \left(\frac{\gamma_\rho}{\gamma_\omega}\right)^2 2\rho_{11}^H \frac{d\sigma}{dt}(\pi^o p \to \omega p)$$

$$+ 2\left(\frac{\gamma_\rho}{\gamma_\omega}\right)\sum_{\lambda=\pm 1}\text{Re}\left[A_\lambda(\pi^o p \to \rho^o p) A_\lambda^*(\pi^o p \to \omega p)\right].$$

(6.11)

The situation concerning measurements of $\gamma_\rho^2/4\pi$ and $\gamma_\omega^2/4\pi$ has been summarized;[27] there, it is pointed out that all direct measurements of the $\gamma - \rho$ coupling yield similar values for $\gamma_\rho^2/4\pi$ with a possible difference between measurements where the photon is on its mass shell (e.g., coherent $\gamma + A \to \rho^o + A$) and measurements where the photon is on the ρ^o mass shell (e.g., $e^+ e^- \to \rho^o \to \pi^+ + \pi^-$). However, the latest Orsay measurements[28] find $\gamma_\rho^2/4\pi = 0.66 \pm 0.07$, somewhat higher than the value when Ref. 27 was written. The measurements for $q^2 = 0$ and $q^2 = m_\rho^2$ are now in agreement and we shall use the Orsay values.

One note of caution must be sounded as a recent electroproduction experiment[29] finds $\sigma(\gamma p \to \rho^o p)$ decreasing as q^2 becomes spacelike and more negative, suggesting that $\gamma_\rho^2/4\pi$ may be increasing in this region.

Returning to Eq. (6.11) we next observe that the second term on the right hand side would appear to be small for $|t| \lesssim 0.6(\text{GeV/c})^2$. Data on the isospin related reaction $\pi^+ + n \to \omega + p$ is available for energies less than 9.0 GeV/c. Ref. 30 shows data for $\rho_{11}^H \frac{d\sigma}{dt}(\pi^+ n \to \omega p)$ for laboratory momenta of 4.19, 5.08, 6.95, and 9.0 GeV/c. We have extrapolated this data to 15.0 GeV/c assuming a $p_{LAB}^{-2.25}$ momenta dependence and a t-distribution independent of energy, both suggested by the data below 9.0 GeV/c. The second term in Eq. (6.11) contributes $\approx 2\%$ for

$|t| \simeq 0(\text{GeV/c})^2$, $\simeq 6\%$ for $|t| \simeq 0.3(\text{GeV/c})^2$, and $\simeq 10\%$ for $|t| \simeq 0.6(\text{GeV/c})^2$. We neglect this term in subsequent calculations.

Finally, we consider the third term in Eq. (6.11), the isoscalar-isovector interference term. Information on this term can be obtained by including data on the reaction $\gamma + n \rightarrow \pi^0 + n$. VDM tells us to write an equation like Eq. (6.11) but with the p everywhere replaced with n. We then use isospin invariance to write

$$A_\lambda(\pi^0 p \rightarrow \rho^0 p) = A_\lambda(\pi^0 n \rightarrow \rho^0 n),$$

$$A_\lambda(\pi^0 p \rightarrow \omega p) = -A_\lambda(\pi^0 n \rightarrow \omega n) .$$

Introducing the conventional notation that

$$R = \frac{\dfrac{d\sigma}{dt}(\gamma n \rightarrow \pi^0 n)}{\dfrac{d\sigma}{dt}(\gamma p \rightarrow \pi^0 p)}$$

we arrive at

$$\left(\frac{8}{\alpha}\right)\left(\frac{\gamma_\rho^2}{4\pi}\right)\left(\frac{1+R}{2}\right) \quad \frac{d\sigma}{dt}(\gamma p \rightarrow \pi^0 p) = 2\rho_{11}^H \frac{d\sigma}{dt}(\pi^0 p \rightarrow \rho^0 \omega) \qquad (6.12)$$

Fig. 28 shows recent data on R for 4.7 GeV/c and 8.2 GeV/c incident photon momenta.[31] This data suggests that $R \rightarrow 1$ as k_γ increases and that $R \gtrsim 0.9$ at 8.2 GeV/ for $|t| \lesssim 0.6$ $(\text{GeV/c})^2$. We thus approximate $R = 1$ at 15.0 GeV/ which evidentally introduces no more than a 5% uncertainty in Eq. (6.12).

Fig. 29 shows the comparison of the two sides of Eq. (6.12); 15.0 GeV/c data from SLAC[32] has been used for $\frac{d\sigma}{dt}(\gamma p \rightarrow \pi^0 p)$. We have also made the approximation that $\rho_{11}^H \simeq 1$ for our data. As discussed in Section B of this chapter, $\rho_{11}^H \simeq 1$ is expected on general grounds and is consistent with our data. The comparison shows qualitative similarity in shape but an overall large normalization difference
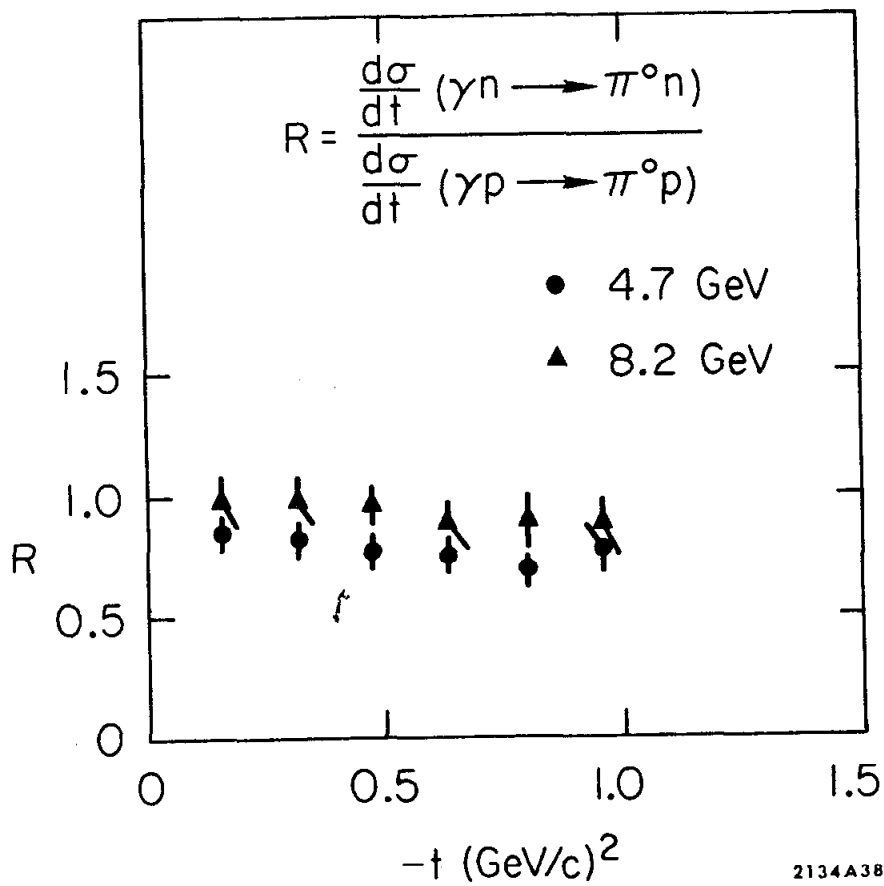
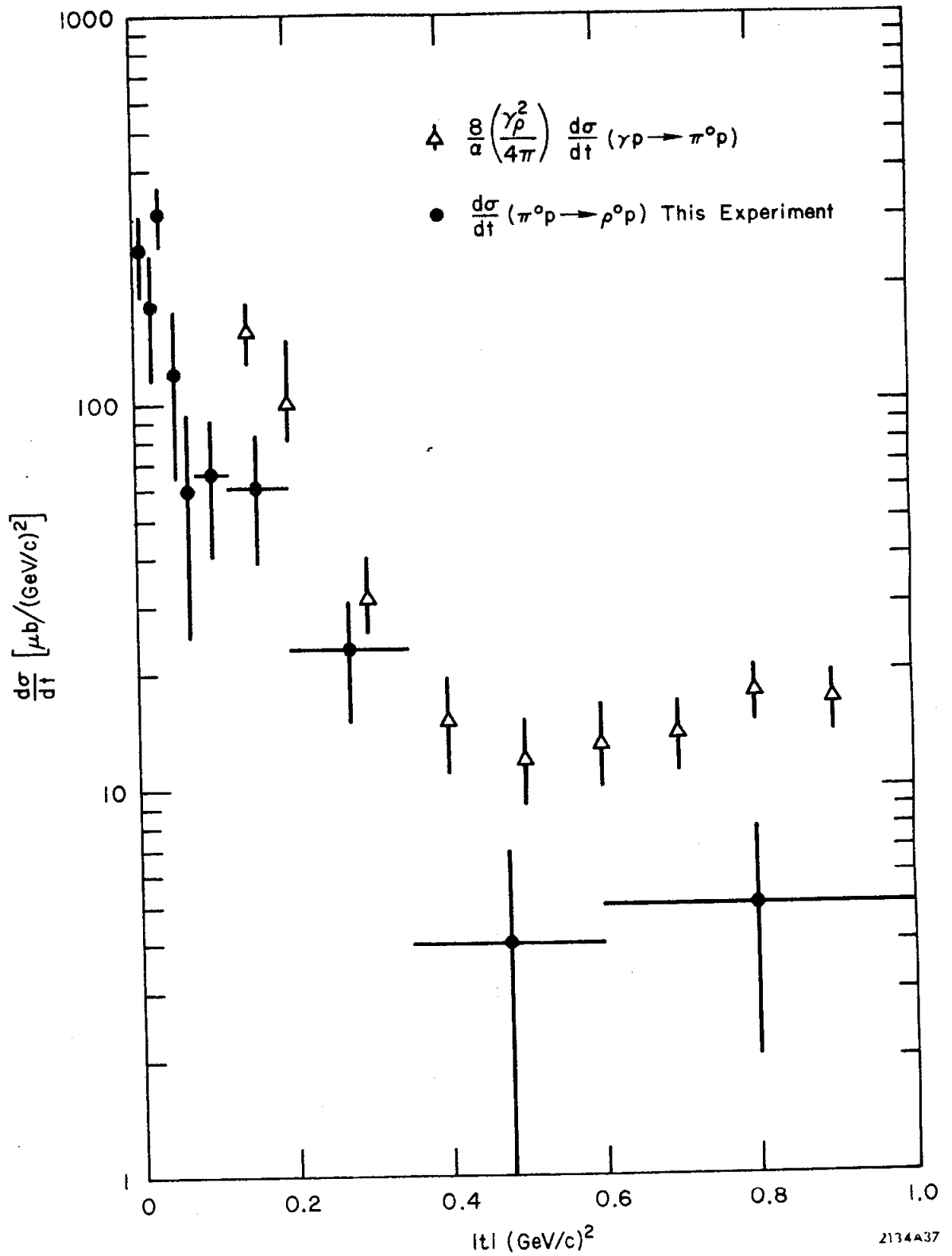FIG. 28--The ratio of π^0 photoproduction from neutrons and protons as a function of momentum transfer.

2134A38

FIG. 29--A comparison of $\gamma p \to \pi^0 p$ and $\pi^0 p \to \rho^0 p$ as a test of the vector dominance model.

which cannot be accounted for by any known systematic effect in our data (see Table 11).

This discrepancy could arise because of the use of an incorrect value of $\gamma_\rho^2/4\pi$. If we let our data determine $\gamma_\rho^2/4\pi$ we find

$$\frac{\gamma_\rho^2}{4\pi} \approx 0.35.$$

This is especially interesting because other experiments relating photo-production reactions to their hadronic counterparts also tend to find lower values of $\gamma_\rho^2/4\pi$.[27] For example, one test of VDM is to check the equality

$$\left(\frac{8}{\alpha}\right)\left(\frac{\gamma_\rho^2}{4\pi}\right)\left(\frac{1+R}{2}\right)\frac{d\sigma}{dt}(\gamma p \to \pi^+ n) = 2\rho_{11}^H \frac{d\sigma}{dt}(\pi^- p \to \rho^0 n) \qquad (6.13)$$

$$R_1 = \frac{\frac{d\sigma}{dt}(\gamma n \to \pi^- p)}{\frac{d\sigma}{dt}(\gamma p \to \pi^+ n)}$$

Formally, this is almost identical to our test in Eq. (6.12). However, the dynamics of the particular reactions involved are quite different, as discussed in Chapter I. Yet, a test of Eq. (6.13) at 15.0 GeV/c incident momentum[13, 33] and at very small t has found a qualitative similarity in shape but a normalization difference which can be accounted for by a substantially smaller value of $\gamma_\rho^2/4\pi$.

A fair summary of the situation would seem to be that experiments which are able to isolate the $\gamma - \rho$ coupling find $\gamma_\rho^2/4\pi \approx 0.7$ while experiments which do not isolate this coupling but depend on various arguments as to the size of the other contributions find $\gamma_\rho^2/4\pi \approx 0.3$.[27]

It has been suggested that the existence of additional vector mesons could explain this.[27] In this model our VDM diagram in Fig. 27 would have

to include additional terms corresponding to these additional vector mesons. And, in fact, recent data[34] indicates the existence of a heavy vector meson with a mass of $\simeq 1.6$ GeV and I = 1. However, this enhancement seems to couple predominantly to the $\rho\pi\pi$ system which would preclude its participation in Fig. 27. Thus, the disagreement in Fig. 29 is unresolved and appears to be a serious violation of the Vector Dominance Model.

F. <u>Summary and Conclusions</u>

In summary, we have extracted the cross section and density matrix elements for the reaction $\pi^0 + p \rightarrow \rho^0 + p$ at 15.0 GeV/c. This data exhibits no signs of the presence of unnatural parity exchanges and is consistent with the basic characteristics expected from ω-exchange; however, the data does not agree with detailed dual-absorption model calculations for ω-exchange. There is disagreement between this experiment and a 16.0 GeV/c bubble chamber experiment.

The energy dependence of the cross section for ω-exchange determines the intercept of the ω-trajectory, $\alpha(o)$; we find $\alpha(o) = 0.42 \pm 0.13$, in agreement with other measurements. Finally, the relation between the processes $\gamma + p \rightarrow \pi^0 + p$ and $\pi^0 + p \rightarrow \rho^0 + p$ was investigated as a test of the Vector Dominance Model. We find qualitative agreement in shape but a significant normalization discrepancy consistent only with a lower value of $\gamma_\rho^2 / 4\pi$ than is currently obtained from direct measurements of the $\gamma - \rho$ coupling.

At the present time three bubble chamber experiments and one spark chamber experiment (this experiment) on $\pi^0 + p \rightarrow \rho^0 + p$ have been reported. What conclusions can one reasonably make about the relative merits of the two methods based on this experience?

At all but the lowest values of t, the spark chamber has a significant

advantage in that it views not only the proton, as the bubble chambers do, but also the two phtons from the π^o decay. This extra information provides for a more complete separation of the ρp signal from the background than is possible in bubble chamber experiments. This feature becomes especially important at high energies. The signal to noise ratio is even more enhanced in the spark chamber method because of the triggerability not present in the normal bubble chamber experiment.

At low-t the two methods are in disagreement, as discussed in Chapter V. This is clearly seen in $d\sigma/dt\,(\pi^\pm p \to \rho^\pm p)$. These general features are propagated into our $\pi^o + p \to \rho^o + p$ data. The bubble chambers may produce dips in $d\sigma/dt\,(\pi^\pm p \to \rho^\pm p)$ because of scanning losses whereas the spark chamber method may fill in dips because of a lack of signal to noise resolution due to the absence of a measurement of the recoil proton angle.

In fact, our result for $d\sigma/dt(\pi^o p \to \rho^o p)$ may be criticized in the low-t region on fairly general grounds. For $t' = \left| t - t_{min} \right|$ small, angular momentum conservation requires that scattering amplitudes have a leading behavior in t' as follows:[35]

$$A_\lambda \propto |t'|^{\frac{n}{2}}$$

Here, n is the total helicity flip. We have argued in Section B of this chapter that the helicity changes by 1 at the boson vertex. Vector Dominance tells us that the ωpp coupling is largely vector, and at high energies vector couplings do not change the helicity.[36] Thus, we would expect a leading behavior of $|t'|$ in $d\sigma/dt(\pi^\pm p \to \rho^\pm p)$, predicting a dip as $t' \to 0$. As we concluded in Chapter V, the low-t behavior must be regarded as unresolved at the present time.

Perhaps, the most fruitful approach would be to combine the advantages of the two methods in a hybrid bubble chamber-spark chamber experiment.

REFERENCES

1. P: B. Johnson et al., Phys. Rev. <u>176</u>, 1651 (1968);

   J. A. Poirier et al., Phys. Rev. <u>163</u>, 1462 (1967);

   B. D. Hyams et al., Nucl. Phys. <u>B7</u>, 1 (1968);

   H. H. Williams, <u>Report No. SLAC-142, Stanford Linear Accelerator</u>

   <u>Center</u>, (1971); Reference 15.

2. G. Grayer et al., <u>Proceedings of the Fourth International Conference</u>

   <u>on High Energy Collisions, Oxford, England, 1972.</u>

3. A. P. Contogouris et al., Phys. Rev. Letters <u>19</u>, 1352 (1967).

4. A. Dar and V. F. Weisskopf, Phys. Rev. Letters <u>20</u>, 762 (1968).

5. L. Dilella, <u>Proceedings of the Lund International Conference on</u>

   <u>Elementary Particles, Lund, Sweden, 1969.</u>

6. W. Michael and G. Gidal, Phys. Rev. Letters <u>28</u>, 1475 (1972).

7. J. P. Baton and G. Laurens, Nucl. Phys. <u>B21</u>, 551 (1970).

8. D. J. Crennell et al., Phys. Rev. Letters <u>27</u>, 1674 (1971).

9. Haim Harari, Phys. Rev. Letters <u>26</u>, 1400 (1971).

10. J. Bartsch et al., Nucl. Phys. <u>B46</u>, 46 (1972).

11. Robert Yamartino, private communication.

12. SLAC User's Note No. 8, (September, 1967).

13. B. N. Ratcliff, <u>Report No. SLAC-141, Stanford Linear Accelerator Center</u>,

    (1971).

14. E. Flaminio et al., <u>CERN/HERA 70-7</u> (1970).

15. F. Bulos et al., Phys. Rev. Letters <u>26</u>, 1453 (1971).

16. M. Jacob and G. C. Wick, Ann. Phys. <u>7</u>, 404 (1959).

17. K. Gottfried and J. D. Jackson, Nuovo Cimento <u>34</u>, 735 (1964).

18. J. D. Jackson, Nuovo Cimento 34, 1644 (1964).

19. O. Skjeggestad, Proceedings of the 1964 Easter School for Physicists, Vol. 2.

20. J. C. Pratt et al., Phys. Letters 41B, 383 (1972); this reference gives a list of all sources used in Fig. 22.

21. G. Giacomelli, Proceedings of the Sixteenth International Conference on High Energy Physics, Batavia, Illinois, 1972.

22. G. Cohen-Tannoudji, Ph. Salin, and A. Morel, Nuovo Cimento 55B, 412 (1968).

23. J. Ballam et al., Phys. Rev. D5, 545 (1972).

24. J. K. Storrow, "Regge Theory for Experimentalists," Daresbury Lecture Note Series No. 6 (1971).

25. A. D. Brody et al., Phys. Rev. Letters 26, 1050 (1971).

26. N. M. Kroll, T. D. Lee, and B. Zumino, Phys. Rev. 157, 1376 (1967).

27. D. W. G. S. Leith, "Lectures to the Scottish Universities Summer School in Physics", Report No. SLAC-PUB-1041, SLAC (1970).

28. J. Lefrancois, Proceedings of the 1971 International Symposium on Electron and Photon Interactions at High Energies, Cornell, 1971.

29. J. T. Dakin et al., Phys. Rev. Letters 30, 142 (1973);
    J. T. Dakin et al., Report No. SLAC-PUB-1211, SLAC (March, 1973) (submitted to Phys. Rev.).

30. F. D. Gault, A. D. Martin, and G. L. Kane, Nucl. Phys. B32, 429 (1971).

31. A. M. Osborne et al., Phys. Rev. Letters 29, 1621 (1972);
    A. M. Osborne et al., CLNS-189, (July, 1972).

32. R. Anderson et al., Phys. Rev. D1, 27 (1970).

33. F. Bulos et al., Phys. Rev. Letters 26, 1457 (1971).

34. M. Davier, <u>Proceedings of the Sixteenth International Conference on High Energy Physics, Batavia, Illinois, 1972.</u>

35. G. L. Kane and Marc Ross, Phys. Rev. <u>177</u>, 2353 (1969).

36. James D. Bjorken and Sidney D. Drell, <u>Relativistic Quantum Mechanics,</u> (McGraw-Hill, New York, 1964).